

# Three-dimensional coupling between Boussinesq (FEM) and Navier-Stokes (particle based) models for wave structure interaction

Shagun Agarwal\*, V. Sriram, K. Murali

Department of Ocean Engineering, Indian Institute of Technology Madras, India

---

## Abstract

The paper presents coupling between a mesh-based finite-element model for Boussinesq equations (FEBOUSS [1]) with a meshless local Petrov-Galerkin model for the Navier-Stokes equations (MLPG\_R [2]) in 3D. Boussinesq equation models are widely used for simulating wave-propagation over large domains with uneven topography using a 2D surface mesh. Mesh-less models inherently capture large free-surface deformations and have shown promise in simulating wave-structure interaction, run-up and breaking phenomenon. The hybrid approach in this paper assumes a 3D MLPG\_R sub-domain surrounded by the 2D mesh of FEBOUSS. The coupling interface in MLPG\_R consists of relaxation zones that can be placed along multiple boundaries of the sub-domain for exchanging particle velocity from FEBOUSS. This hybrid model is therefore capable of simulating directional waves, that has not been reported previously.

The paper first presents the procedure for calculating the depth-resolved velocities in 3D from the Boussinesq model. The resultant velocities are compared against theory, experiments and other models. The following sections present the coupling algorithm along a single and multiple coupling interfaces in MLPG\_R. Validation results for this hybrid model are provided using surface elevation and velocity measurements for regular waves, including directional cases. In general, the results from the hybrid model are reported to have marginal over-prediction of peaks compared to purely MLPG\_R simulation. Finally, the interaction of a vertical cylinder with direction regular wave is simulated using the 3D hybrid model.

Manuscript accepted in Ocean Engineering

Published version at <https://doi.org/10.1016/j.oceaneng.2022.112426>

Cite as :

Agarwal, S., Sriram, V., Murali, K. (2022). Three-dimensional coupling between Boussinesq (FEM) and Navier-Stokes (particle based) models for wave structure interaction. *Ocean Engineering*, 263, 112426, ISSN 0029-8018.

<https://doi.org/10.1016/j.oceaneng.2022.112426>

© 2022 This manuscript version is made available under the CC-BY-NC-ND 4.0 

**Keywords:** Boussinesq equation, Finite element method, Hybrid modelling, Mesh-free method, MLPG, Free-surface flow

---

## 1. Introduction

Numerical modelling of wave-structure interaction is an important tool in the design, installation and operation of coastal and offshore systems. Over decades of research, a large number of models have been developed using various governing equations, assumptions and numerical methods. However, simulation of realistic large domain problems using a single numerical model is often a compromise between prohibitive computational effort and accuracy. The physics of majority of the domain may be captured by potential flow assumption, while the viscous flow may be relevant only in local regions around structures or breaking waves. Lately, significant research has been

focused on coupling two or more numerical models to create a hybrid approach that can enhance their individual strengths while minimising their shortcomings. This was highlighted in a recently concluded comparative study on modelling the interaction of focusing waves with vertical cylinder [3], where majority of the simulations involved some variation of hybrid modelling.

The coupling methods can be broadly classified into functional decomposition and domain decomposition. In the functional decomposition approach, the Navier-Stokes equations are split into two components, an irrotational part and a complementary rotational part. The irrotational equations are solved in the complete domain. The complementary equations are solved in the viscous regions, while assuming a zero value in the remaining portion. A popular example of this method relevant to ocean engineering problems is the SWENSE model, which

---

\*Corresponding author

Email address: shagun.1994@gmail.com (Shagun Agarwal)

has been applied for simulating sea-keeping response of floating body [4, 5].

Most commonly, the hybrid models are developed using domain decomposition approach, where different regions of the domain are simulated using different models depending on the flow characteristics. The propagation and transformation of non-breaking waves over large domains is usually modelled using potential flow models. These include fully-resolved nonlinear potential theory (FNPT) models such as QALE-FEM [6], IITM-FNPT [7], OceanWave3D [8]; or depth-averaged Boussinesq-type equations models such as FUNWAVE [9], COULWAVE [10]; or nonlinear shallow-water equation models such as SWASH[11]; or spectral methods such as HOS [12] and enhanced spectral boundary integral method (ESBI) [13]. On the other hand, a three-dimensional dynamic viscous flow in region around structures or breaking waves should be simulated using Navier-Stokes models. These include Eulerian two-phase model OpenFOAM [14] for laminar or turbulent flows based on RANS, and LES based turbulence models [15, 16] applied to ocean engineering. The viscous flow can also be modelled using Lagrangian single-phase models such as SPH [17, 18], MLPG\_R [19, 2] and MPS [20]. Many of these models have been used in contemporary literature for developing hybrid models, as listed in Table 1. Alternatively, the Lattice Boltzmann (LB) method treats the fluid as field of particle distribution functions [21], capable of efficient parallel implementation [22]. The LB method was coupled with boundary element method based FNPT for simulating breaking solitary wave in [23].

Apart from the constituent models, the unique characteristics of a hybrid model are dependent on the coupling interface. The coupling interface is the region for transferring information between the two models. One zone is considered to be modelled by Navier-Stokes equation. The other zone may be modelled using fully non-linear potential theory (FNPT), weakly non-linear potential theory, Boussinesq equations or nonlinear shallow water equation (NSWE). This paper is primarily concerned with one-way coupling, where the wave information is given from other models to the Navier-Stokes model. Further, it is assumed that the waves within the coupling interface are non-breaking. It should be noted that there may be differences in the numerical solution of the same wave between various models. This is especially true for the wave-kinematics. For example, the wave-kinematics obtained from a FNPT model and a Navier-Stokes model may only have a marginal difference for non-breaking waves. However, the wave kinematics for a steep wave obtained using a perturbation-method based formula from a depth-integrated Boussinesq equation model such as FEBOUSS (see section 3.1), may have significant differences compared to a Navier-Stokes model. Further, the Navier-Stokes zone may contain structures that influence the incoming wave and may require to be treated by the coupling interface. Therefore, in order to maintain the consistency of the combined solution, different coupling interface algorithms have been developed depending on the models.

Following the classifications in [24] and [25], the coupling interface approaches can be categorised as moving or station-

ary boundary wall, overlapping relaxation zone or open boundary condition, as shown in Fig. (1). Table 1 lists a few references where each method has been applied. A fixed boundary is usually applied between two fixed-mesh (Eulerian) models, where wave information is passed through Dirichlet boundary condition, usually for both velocity and pressure governing equations. This type of coupling interface may be present along a number of domain boundaries. The use of self-adaptive wave generation methods allows active absorption of reflected waves generated by the presence of structures [26]. A 2D hybrid model using this approach was presented in [27], with two-way coupling using a single fixed boundary between finite-difference models for 1DH Boussinesq equation and 2D Navier-Stokes equation.

Alternatively, a moving boundary may be required for coupling a mesh-based model with a particle-based model. In variations of this approach, the boundary may be moved using only horizontal or all components of the flow velocity. This interface is usually applied along one boundary [30], but it may be applied along two non-intersecting boundaries, as done in [29] in a 2D domain. However its implementation in 3D with intersecting moving boundaries will be challenging. Further, as described in [29], this method uses changes in local particle-number density in the vicinity of the moving boundary for driving the wave and hence can only be used in particle-based methods using density-invariant or weakly compressible forms of the pressure Poisson equation (PPE) (see section 2.2). It should be noted, [29] also reports that this mechanism is responsible for the noise in the wave-kinematics obtained from the hybrid model. When applied to divergence-free forms of PPE, this method leads to 'leakage' of particles as reported in [33]. Finally, this approach too cannot absorb a reflected wave in one-way coupling.

The relaxation zone method has overlapping region where the flow quantities are gradually ramped between the two models using a relaxation function. This method hence provides abundant flexibility in its implementation through choice of fixed or moving relaxation region, choice of ramping function, size of relaxation zone and the choice of the coupled quantities. Conventionally, a flow quantity  $\Phi$  in the relaxation zone is defined by a linear combination of the solutions  $\Phi^A$  and  $\Phi^B$  from the two models,  $\Phi = C\Phi^A + (1 - C)\Phi^B$ . Here,  $C$  is a smooth relaxation function defined using polynomial or hyperbolic function of spatial coordinates within the relaxation zone. Due to the presence of a relaxation zone, ideally this method is capable of absorbing differences between the solutions from the two models and reflections from structures. However, similar to a sponge layer, a certain amount of re-reflection from the relaxation region should be expected, which can be minimised through tuned choice of relaxation function and size of the relaxation zone [32]. Further, the flow within the relaxation zone is not expected to satisfy the governing equations of either model. For example, if the models being coupled are incompressible, individually the divergence of velocity will be equal to zero for both of them. However their combined velocity vector within the relaxation zone may have non-zero divergence. Further, this value will be proportional to the difference in their

Table 1: Table listing examples for various implementations of coupling interface in contemporary literature.

	Reference	Coupling Interface	Model Other	Model Navier-Stokes
1	Sitanggang and Lynett (2009) [27, 28]	Boundary Fixed	Boussinesq-1D Mesh Eul, FDM	RANS 2D Mesh Eul, FDM
2	Verbrugge et al. (2018) [29]	Boundary Moving	OceanWave3D FNPT Mesh Eul, FDM	SPHysics 2D Particle Lag, SPH
3	Narayanaswamy et al. (2010) [30]	Boundary Moving	FUNWAVE Boussinesq-1D Mesh Eul, FVM-FDM	SPHysics 2D Particle Lag, SPH
4	Wang et al. (2020) [31]	RZ Fixed	QALE-FEM FNPT-3D Mesh Eul-Lag, FEM	OpenFOAM 3D Mesh Eul, FVM-FDM
5	Altomare et al. (2018) [32]	RZ Fixed	SWASH NSWE-1D Mesh Eul, FDM	DualSPHysics 2D Particle Lag, SPH
6	Sriram et al. (2014) [24]	RZ Moving	IITM-FNPT FNPT-2D Mesh Eul Lag, FEM	2D Particle Lag, MLPG_R
7	Agarwal et al. (2021) [2]	RZ Moving	IITM-FNPT FNPT-2D Mesh Eul Lag, FEM	3D Particle Lag, MLPG_R
8	Ni et al. (2020) [25]	OBC Fixed	NSWE Mesh Lag, SPH	2D Particle Lag, SPH

RZ = Relaxation zone, OBC = Open boundary condition

FNPT = Fully non-linear potential theory, NSWE = Nonlinear shallow water equation

Eul = Eulerian, Lag = Lagrangian

FDM = Finite difference method, FVM = Finite volume method

FEM = Finite element method, SPH = Smoothed particle hydrodynamics

MLPG\_R = Meshless local Petrov-Galerkin

velocities and the gradient of the relaxation function, as shown in the following equation.

$$\vec{u} = C\vec{u}^A + (1 - C)\vec{u}^B \quad (1a)$$

$$\nabla \cdot \vec{u} = \nabla C \cdot (\vec{u}^A - \vec{u}^B) \quad \text{assuming } \nabla \cdot \vec{u}^A = 0, \nabla \cdot \vec{u}^B = 0 \quad (1b)$$

Finally, multiple relaxation zones can be placed along intersecting boundaries or even inside a domain, making this method convenient for a 3D application.

The work in [31] presents one-way coupling between a meshed 3D FNPT and meshed 3D Navier-Stokes model with fixed relaxation zones along three boundaries using a polynomial relaxation function and all components of velocity  $\vec{u}$  and pressure. On the other hand [32] uses a single fixed relaxation zone with hyperbolic relaxation function and only horizontal velocity as a wave-making condition in a particle-based model

with input from nonlinear SWE. The work in [32] has presented a detailed analysis on performance of the relaxation zone in absorbing the reflection of various regular waves by varying the coefficients of the hyperbolic relaxation function and size of the relaxation zone. A two-way coupling in 2D [24] and one-way coupling in 3D [2] between a meshed FNPT and particle-based MLPG\_R models were implemented using a single moving relaxation zone with a cubic relaxation function. In these works all components of  $\vec{u}$  and pressure were used for coupling due to the excellent agreement between the solvers for non-breaking waves. An open boundary condition was proposed in [25] for inlet and outlet of waves in particle-based SPH. This method was used for coupling SPH in 2D with a shallow-water model. The approach relies on creation and deletion of particles in a buffer zone and does not require a gradual ramping of the solution in the coupling interface. However, similar to the moving boundary approach, this method may not be applicable to

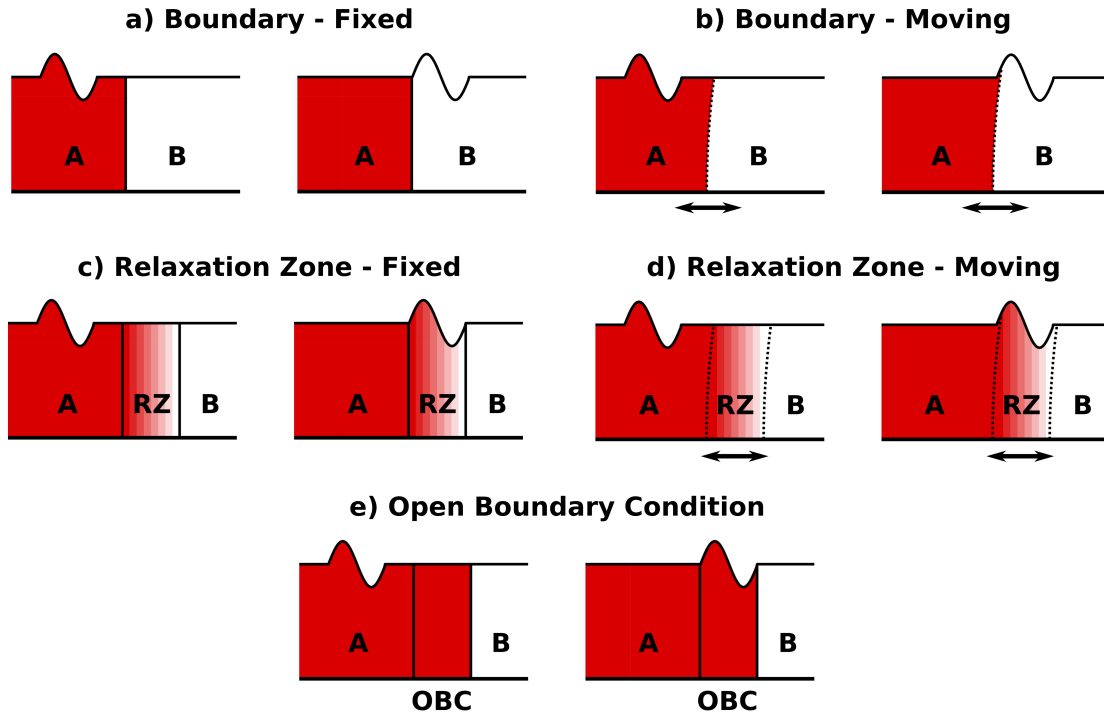


Figure 1: Schematic showing various implementations of coupling interface in contemporary literature for transferring waves from domain A to domain B modelled by different equations and different numerical methods. Please refer to Table 1 for examples of each approach in the contemporary literature.

divergence-free form of PPE. These few examples demonstrate the versatility of relaxation zone methods in hybrid modelling.

The literature currently lacks three-dimensional coupling between a mesh-based Boussinesq equation model and a mesh-less Navier-Stokes model. These two categories of models have significantly different formulations. Due to this, it's fairly challenging to couple these two models, but it provides an opportunity for combining distinctly different strengths and minimising their major weaknesses for practical application. This work presents one-way 3D coupling between a Boussinesq equation model, named FEBOUSS [1] and a mesh-less Navier-Stokes model, referred to as MLPG\_R [2, 34] in this manuscript. FEBOUSS is a finite-element model for depth-integrated form of Boussinesq equation. Models in this category can capture the 3D wave-transformation using a 2D surface mesh, thus enabling efficient analysis of wave transformation over large domains. However, they cannot be directly applied for viscous flow around 3D structures and wave-breaking. The mesh-less MLPG\_R model solves the Lagrangian form of governing equations [34]. Here the domain is discretised using moving particles, and thus it can directly capture a moving free-surface. However, the computational cost of this method limits its widespread application. The proposed hybrid model will simulate majority of the domain using FEBOUSS, with local sub-domain of MLPG\_R in the vicinity of structures. This approach can enable simulation of realistic problems using particle-based method.

The paper briefly presents the governing equations and numerical formulation for both FEBOUSS and MLPG\_R models. Section 3.1 describes calculation of depth-resolved veloc-

ities from the depth-integrated results of FEBOUSS. The following section 3.2 presents the construction of the coupling interface within the MLPG\_R sub-domain using relaxation and buffer zones to enable consistent 3D transfer of velocities from FEBOUSS. These developments are investigated using a number of numerical tests. Section 4.1 present a comparison of depth-resolved quantities from FEBOUSS against theoretical and other numerical results. This is crucial for determining and justifying the choice of variables to be transferred in the coupling interface. The algorithm is further validated against experimental results on depth-resolved velocity under waves passing over a submerged bar in section 4.2. The hybrid model is then tested for wave-input from FEBOUSS to MLPG\_R sub-domain using single and two coupling interfaces in section 4.3. It investigates the required setup and compares the results for surface elevation and velocities from the hybrid model against purely FEBOUSS and purely MLPG\_R results. Similar analysis is further carried out for the directional wave case in section 4.5. Building upon the inferences from these trials, the final section 4.6 applies hybrid model for simulating interaction of a directional regular wave with a vertical cylinder, and presents a comparison for pressure and wave probes against purely MLPG\_R and experimental results.

## 2. Governing Equations

The three dimensional numerical domain is defined on a Cartesian coordinate system,  $OXYZ$ , with  $z = 0$  at mean-sea level and the  $Z$  axis positive along the vertically upward direction. The depth-integrated Boussinesq equation model spans

the domain in the  $XY$  plane.

### 2.1. Boussinesq equation model: FEBOUSS

The model is based on Madsen and Sorensen's form of Boussinesq equations for slowly varying bathymetry, as presented in [35]. The flow is assumed to be irrotational, incompressible and inviscid. This depth-integrated form is weakly-nonlinear and weakly-dispersive, with excellent shoaling and linear dispersion characteristics for waves up to  $kh = 3$ . Here  $k = 2\pi/L$  is the wave number,  $h$  is the still water depth and  $L$  is the wave-length. These equations can model 3D wave-transformation in intermediate and shallow depths using a 2D surface mesh, making this a computationally efficient approach for large domains. This category of equations are also referred to as two-dimensional horizontal (2DH) models. Eq. (2) is the complete governing equation, where Eq. (2a) is the continuity equation, and Eqs. (2b) and (2c) are the  $X$  and  $Y$  momentum equations, respectively. The variables here are still water-depth  $h$ , surface-elevation  $\eta$ , total water depth  $d = \eta + h$ , depth-integrated velocity  $P = \int_{-h}^{\eta} u_x dz$  and  $Q = \int_{-h}^{\eta} u_y dz$  along  $X$  and  $Y$  axis respectively, acceleration due to gravity  $g$  and density of water  $\rho$ . The additional terms  $\Psi_1$  and  $\Psi_2$  in the momentum equations are the high-order dispersive terms defined by Eqs. (3a) and (3b) respectively. Here  $\omega$  is an auxiliary variable governed by Eq. (3c), which is required for resolving the third-order spatial derivatives of  $\eta$ . Finally,  $\tau_1, \tau_2$  are the bottom shear stress terms defined by the quadratic friction law. For further details regarding the governing equations, please refer to [36].

$$\frac{\partial \eta}{\partial t} + \frac{\partial P}{\partial x} + \frac{\partial Q}{\partial y} = 0 \quad (2a)$$

$$\frac{\partial P}{\partial t} + \frac{\partial}{\partial x} \left( \frac{P^2}{d} \right) + \frac{\partial}{\partial y} \left( \frac{PQ}{d} \right) + gd \frac{\partial \eta}{\partial x} + \Psi_1 + \frac{\tau_1}{\rho} = 0 \quad (2b)$$

$$\frac{\partial Q}{\partial t} + \frac{\partial}{\partial x} \left( \frac{PQ}{d} \right) + \frac{\partial}{\partial y} \left( \frac{Q^2}{d} \right) + gd \frac{\partial \eta}{\partial y} + \Psi_2 + \frac{\tau_2}{\rho} = 0 \quad (2c)$$

$$\begin{aligned} \Psi_x = & - \left( B + \frac{1}{3} \right) h^2 \left( \frac{\partial^3 P}{\partial x^2 t} + \frac{\partial^3 Q}{\partial x y t} \right) - h \frac{\partial h}{\partial x} \left( \frac{1}{3} \frac{\partial^2 P}{\partial x t} + \frac{1}{6} \frac{\partial^2 Q}{\partial y t} \right) \\ & - h \frac{\partial h}{\partial y} \left( \frac{1}{6} \frac{\partial^2 Q}{\partial x t} \right) - Bgh^2 \frac{\partial w}{\partial x} \end{aligned} \quad (3a)$$

$$\begin{aligned} \Psi_y = & - \left( B + \frac{1}{3} \right) h^2 \left( \frac{\partial^3 P}{\partial x y t} + \frac{\partial^3 Q}{\partial y^2 t} \right) - h \frac{\partial h}{\partial y} \left( \frac{1}{6} \frac{\partial^2 P}{\partial x t} + \frac{1}{3} \frac{\partial^2 Q}{\partial y t} \right) \\ & - h \frac{\partial h}{\partial x} \left( \frac{1}{6} \frac{\partial^2 P}{\partial y t} \right) - Bgh^2 \frac{\partial w}{\partial y} \end{aligned} \quad (3b)$$

$$\omega = \frac{\partial}{\partial x} \left( h \frac{\partial \eta}{\partial x} \right) + \frac{\partial}{\partial y} \left( h \frac{\partial \eta}{\partial y} \right) \quad (3c)$$

The finite element model is constructed on an unstructured mesh of irregular triangles. We use a mixed formulation, with

linear shape function for  $\eta$  and  $\omega$ , and quadratic shape function for  $P$  and  $Q$ . This use of unequal order basis functions is required for avoiding spurious oscillations in the solution [36]. The weak form is evaluated using the standard Galerkin method. The expressions for elemental integrals are calculated analytically using symbolic computation in Mathematica [37], instead of the tradition Gauss quadrature approach. The time-marching is implemented at a constant time-step using Runge-Kutta 4<sup>th</sup> order scheme (RK4) due to its low truncation error  $O(\Delta t^5)$ . This time-step is prescribed using the Courant number  $Cou = \max\{\frac{\Delta t}{\Delta r} \sqrt{gh}\}$ , where a condition of  $C \leq 1$  is usually sufficient for a stable simulation. The final discretised set of algebraic equations is solved using an iterative bi-conjugate gradient stabilised solver (BiCGStab) for sparse matrices.

The domain boundaries in the model can be slip walls, where  $P_n = Pn_x + Qn_y$ ; or no-slip walls, where  $P = 0, Q = 0$ . Further, waves in the domain can be generated from a boundary using the Dirichlet method, where the Fourier series solution for Boussinesq equations at constant depth in 1D [38] is used for prescribing the  $\eta, P$  and  $Q$  velocity time-series. Finally, the outgoing waves are absorbed using Newtonian cooling based sponge layers. For complete details regarding the FEM formulation and boundary conditions, please refer to [1].

This model, named FEBOUSS, was validated against the standard Whalin shoal [39] test for non-linear refraction and diffraction of regular waves over the semi-circular shoal in [1] through wave-elevation measurements. The model was also tested against the Berkhoff shoal [40] bathymetry, which consists of an angled shoal with an ellipsoidal hump. The validation was done in [41] through wave-height measurements along various sections downwind of the ellipsoid. The model was applied for simulating flow of solitary waves through porous breakwaters in [41]. Further, FEBOUSS was extended for simulating ship-generated waves, through the implementation of a moving pressure field. This was presented and validated in [1] against field measurements of waves generated by fast-moving ferries in Tallinn bay, Estonia. In this hybrid modelling work, FEBOUSS will be used for the generation and propagation of waves over large distances with variable bathymetry, where the flow is largely potential.

It should be noted that the weakly dispersive governing equation in FEBOUSS limit its application to intermediate water-depth  $kh = 3$ . Further, the results in [42] highlight the limitation of weakly dispersive Boussinesq models in replicating focusing waves, especially with a wide-band spectrum. However, these models are still applicable to the wide range of near-shore and coastal applications. The limitations of weakly dispersive models have been addressed by high-order and multi-layer forms of Boussinesq equation. The resultant models can offer improved nonlinear properties and provide inherent expressions for vertical variation of quantities, for waves ranging from shallow to deep water-depths. For example, [43] formulated a 1DH two-layer Boussinesq model that can provide accurate wave-wave interaction and horizontal and vertical velocities up-to  $kh=23.2$ . The finite difference model for its 1DH form was presented in [44]. Another recent example is the multi-layer approach in [45], which formulates the depth-integrated equations in  $\sigma$ -

coordinate system and uses the Galerkin or sub-domain method to minimise the residual in the momentum equation. However, the extension of these models to 2DH is lengthy, introduces additional governing equations and would require further research for a stable finite-element formulation. Therefore, the analysis in this manuscript will be limited to intermediate water-depth, as per the constraints of FEBOUSS.

## 2.2. Navier-Stokes model: MLPG\_R

The Navier-Stokes equation for incompressible laminar flow in Lagrangian form in a three-dimensional domain  $\Omega$  is given by Eq. (4), where Eq. (4a) is the continuity and Eq. (4b) is the momentum governing equation. Here  $\vec{u} = u\hat{i} + v\hat{j} + w\hat{k}$ , where the velocity vector  $\vec{u}$  has components  $u, v, w$ . Further,  $p$  is the pressure,  $\rho$  is the fluid density,  $\nu$  is the kinematic viscosity of the fluid and  $\vec{g} = -9.81\hat{k}$  is the body force vector.

$$\nabla \cdot \vec{u} = 0 \quad \text{in } \Omega \quad (4a)$$

$$\frac{D\vec{u}}{Dt} = \frac{-\nabla p}{\rho} + \vec{g} + \nu \nabla^2 \vec{u} \quad \text{in } \Omega \quad (4b)$$

This governing equation is solved using the projection scheme to decouple the pressure gradient and momentum equation. Given the values of flow velocity  $\vec{u}^n$  at time-step  $n$  are known, the first step is to remove the pressure gradient term from the momentum equation to obtain the intermediate velocity  $\vec{u}^*$  by Eq. (5a). Once the pressure has been calculated, the flow velocity  $\vec{u}^{n+1}$  at next time-step  $n+1$  can be recovered using the corrector equation Eq. (5b). The governing pressure Poisson equation (PPE) Eq. (6) is obtained by taking the gradient of Eq. (5b) and using the continuity equation Eq. (4a). In contemporary literature, Eq. (6) is often referred to as the divergence-free form. Alternatively, several incompressible particle based methods use a density-invariant form [46] of the PPE that uses the local particle-number density instead of intermediate velocity.

$$\vec{u}^* = \vec{u}^n + \Delta t \left( \vec{g} + \nu \nabla^2 \vec{u}^n \right) \quad \text{in } \Omega \quad (5a)$$

$$\vec{u}^{n+1} = \vec{u}^* - \Delta t \frac{1}{\rho} \nabla p^{n+1} \quad \text{in } \Omega \quad (5b)$$

$$\nabla^2 p^{n+1} = \frac{\rho}{\Delta t} \nabla \cdot \vec{u}^* \quad \text{in } \Omega \quad (6)$$

We model these equations using the meshless local Petrov-Galerkin with Rankine source method (MLPG\_R) [34]. This is a particle based method where the numerical domain is spatially discretised using nodes moving at flow velocity. Therefore, this method can inherently capture the moving free-surface and avoids the convection terms in the momentum equation. The sequence to be followed for numerical solution is a) the calculation of the intermediate velocity  $\vec{u}^*$  using Eq. (5a), b) the calculation of pressure  $p^{n+1}$  using Eq. (6), c) the correction of velocity to get  $\vec{u}^{n+1}$  using Eq. (5b), d) updating the node position as

per  $\vec{r}^{n+1} = \vec{r}^n + \vec{u}^{n+1} \Delta t$ . In this model, the intermediate and correction equations Eqs. (5a) and (5a) are solved in 'strong' form, where the spatial gradients are calculated using the simplified finite-difference interpolation (SFDI) method [19]. However, MLPG\_R is unique in solving the pressure Poisson equation in 'weak' form among the meshless methods.

$$\int_{\Omega_I} \psi \nabla^2 p \, d\Omega = \frac{\rho}{dt} \int_{\Omega_I} \psi \nabla \cdot \vec{u}^* \, d\Omega \quad (7a)$$

$$\Rightarrow \int_{\Gamma_I} \lambda_I \cdot (p \nabla \psi) \, d\Gamma - R_I p = \frac{\rho}{\Delta t} \int_{\Omega_I} \vec{u}^* \cdot \nabla \psi \, d\Omega \quad (7b)$$

$$\Rightarrow \frac{1}{6} (p_1 + p_2 + p_3 + p_4 + p_5 + p_6) - p_0 \\ = \frac{\rho}{\Delta t} \frac{R_I}{12} (u_1^* - u_3^* + v_2^* - v_4^* + w_5^* - w_6^*) \quad (7c)$$

For a numerical node  $I$ , the weak form is evaluated in a local spherical sub-domain  $\Omega_I$ , of radius  $R_I$ , with boundaries  $\Gamma_I$ , and having outward unit normal  $\lambda_I$ . Eq. (6) is multiplied with Rankine source test function  $\psi$  [34] and integrated over the sub-domain  $\Omega_I$  to obtain the weak-form Eq. (7a). By using the Gauss theorem, Eq. (7a) can be reduced to Eq. (7b), as shown in [34]. This operation removes the derivative operator from the unknown quantities  $p$  and  $\vec{u}^*$ , and also converts the domain integral to surface integral for the pressure term. Finally through the use Taylor series, Eq. (7b) can be reduced to algebraic form Eq. (7c) with error  $O(R_I^4)$ , resulting in a semi-analytical integration, as shown in [2]. Here, the subscripts in Eq. (7c) denote the values at various locations on the sphere of integration. The details regarding the weak-form and semi-analytical integration are presented in [2].

$$\vec{n} \cdot \nabla p = \rho \left( \vec{n} \cdot \vec{g} - \vec{U} \cdot \vec{n} + \vec{n} \cdot (\nu \nabla^2 \vec{u}) \right) \quad \text{on } \Gamma_w \quad (8a)$$

$$\vec{u} \cdot \vec{n} = \vec{U} \cdot \vec{n} \quad \text{on } \Gamma_w \quad (8b)$$

The three-dimensional numerical domain is bound by three types of boundary conditions (BC), a) wave-maker  $\Gamma_{wm}$  b) free-surface  $\Gamma_{fs}$  c) wall  $\Gamma_w$ . The wave-making BC was implemented in [2] using FNPT input. The free-surface BC, defined by  $p = 0$  on  $\Gamma_{fs}$ , is applied as Dirichlet BC to the pressure Poisson solver. An accurate detection of the free-surface nodes is required to avoid noise in the pressure solution. This was discussed and implemented in [2] using a summated unit vector method for the three-dimensional domain. The wall BC is defined by Eq. (8), where the gradient in the pressure wall BC Eq. (8a) is evaluated using the SFDI method. Finally, the wall BC for velocity, given by Eq. (8b), is implemented using moving side-wall method for the tangential side-walls of the domain, and ghost-mirror particle method for the bluff body boundaries. These techniques are necessary for capturing small amplitude components of focusing waves and are discussed in detail in [2]. Further, the work in [2] also reports convergence

and mass conservation of the order of  $10^{-3}$  through the simulation of fixed cylinder interacting with steep-focusing waves.

The MLPG\_R method has been applied to simulate a variety free-surface flows. It was used for studying the interaction of regular waves with a floating body along with green-water impact in 2D in [47]. This was extended further to simulate the interaction of focusing waves with two fixed bodies in 2D in [48]. With the inclusion of porosity, the attenuation of regular waves over vegetation was simulated in [49]. The 2D MLPG\_R model was coupled with a fully nonlinear potential theory (FNPT) model for simulation of breaking waves [24]. This hybrid model was used for simulating run-up of long waves in [50] and impact of breaking waves on elastic wall in [51]. Finally, the MLPG\_R model in 3D was validated against experimental results for interaction of cylinder with focusing waves in [2, 33]. A complete review of various applications of MLPG\_R model is done in [52]. In this paper, the coupling of 3D MLPG\_R with FEBOUSS can enable its application to practical scale problems.

### 3. Coupling Algorithm

The primary objective of this paper is one-way coupling of FEBOUSS with MLPG\_R in three-dimension. This requires the understanding of two key questions, 1) transfer of variables between the two models 2) ensuring consistency of the solution during coupling. The following sub-sections describe the implementation of coupling algorithm while addressing these key perspectives.

#### 3.1. Calculation of depth-resolved velocities from FEBOUSS

The two models FEBOUSS and MLPG\_R solve for different variables. FEBOUSS is a 2DH model which returns the depth-integrated velocities  $P, Q$  on a XY plane and surface elevation  $\eta$ . On the other hand, MLPG\_R is a 3D model which solves for the flow velocities  $\vec{u} = u\hat{i} + v\hat{j} + w\hat{k}$  and pressure  $p$  in the XYZ domain. Therefore, in order to instantaneously transfer flow variables from FEBOUSS to MLPG\_R, we need to calculate 3D depth-resolved velocities and pressure from the 2DH depth-integrated Boussinesq equations. This requires an explicit expression for depth-resolved quantities in terms of the depth-integrated quantities. The expression will contain high-order spatial derivatives, which are evaluated at the solution nodes and may pose a numerical challenge. This aspect was discussed in [53], where the reconstruction of the velocities from a depth-averaged solution using a finite-difference approach required use of low-pass filtering methods to minimise the noise in the second-order spatial derivative. As shown in section 4.2, such filtering may adversely influence the accuracy of the result. Further, unlike the 2D coupling in contemporary literature [28, 29, 30, 54], the 3D coupling as attempted in this work would require calculation of cross-derivatives. The presented work addresses this numerical complexity by employing a meshless approach for evaluating depth-resolved velocity at the FEM nodes.

For a 2D problem, the vertical structure of horizontal velocity  $u$  was derived in [55] through perturbation method, resulting in

the expected parabolic expression given by the following equation.

$$u = \bar{u} + \left( \frac{h^2}{6} - \frac{z^2}{2} \right) \frac{\partial^2}{\partial x^2}(\bar{u}) - \left( \frac{h}{2} + z \right) \frac{\partial^2}{\partial x^2}(\bar{u}h) \quad (9)$$

Here  $z = 0$  at mean seal level and  $\bar{u} = \frac{P}{h+\eta}$ . The expression was derived by retaining terms with order lower than  $O(\epsilon^2 \mu, \epsilon \mu^2)$ , where  $\epsilon = a/h$  and  $\mu = h/L$  are the non-linearity and dispersion parameters respectively, for a characteristic wave-length  $L$  and amplitude  $a$ . For a 3D problem, this expression was extended in [55] using  $\nabla_h = \frac{\partial}{\partial x}\hat{i} + \frac{\partial}{\partial y}\hat{j}$ , resulting the expressions for  $u$  and  $v$  given by Eqs. (10a) and (10b). Here  $\bar{\mathbf{u}} = \frac{P}{h+\eta}\hat{i} + \frac{Q}{h+\eta}\hat{j}$ . The expressions for  $w$  given by Eq. (10c) and pressure  $p$  given by Eq. (10d) can now be obtained using the continuity equation for irrotational flow and the Z momentum equation, while retaining terms with order lower than  $O(\epsilon^2 \mu, \epsilon \mu^2)$ .

$$u = \frac{P}{h+\eta} + \left( \frac{h^2}{6} - \frac{z^2}{2} \right) \frac{\partial}{\partial x}(\nabla_h \cdot \bar{\mathbf{u}}) - \left( \frac{h}{2} + z \right) \frac{\partial}{\partial x}(\nabla_h \cdot \bar{\mathbf{u}}h) \quad (10a)$$

$$v = \frac{Q}{h+\eta} + \left( \frac{h^2}{6} - \frac{z^2}{2} \right) \frac{\partial}{\partial y}(\nabla_h \cdot \bar{\mathbf{u}}) - \left( \frac{h}{2} + z \right) \frac{\partial}{\partial y}(\nabla_h \cdot \bar{\mathbf{u}}h) \quad (10b)$$

$$\begin{aligned} w = & -\nabla_h \cdot \bar{\mathbf{u}}h - z(\nabla_h \cdot \bar{\mathbf{u}}) - \frac{zh}{3}(\nabla_h h \cdot \nabla_h(\nabla_h \cdot \bar{\mathbf{u}})) \\ & + \frac{z}{2}(\nabla_h h \cdot \nabla_h(\nabla_h \cdot \bar{\mathbf{u}}h)) \\ & - \frac{z}{6}(h^2 - z^2)(\nabla_h \cdot \nabla_h(\nabla_h \cdot \bar{\mathbf{u}})) \\ & + \frac{z}{2}(h+z)(\nabla_h \cdot \nabla_h(\nabla_h \cdot \bar{\mathbf{u}}h)) \end{aligned} \quad (10c)$$

$$p = \rho g (\eta - z) + \rho z \frac{\partial}{\partial t} \left( \nabla_h \cdot \bar{\mathbf{u}}h + \frac{z}{2} \nabla_h \cdot \bar{\mathbf{u}} \right) \quad (10d)$$

Hence for a point  $S(x, y, z)$  in the XYZ domain, the calculation of depth-resolved quantities would require up-to third order spatial derivatives of the Boussinesq solution  $\bar{\mathbf{u}} = \frac{P}{h+\eta}\hat{i} + \frac{Q}{h+\eta}\hat{j}$  at location  $(x, y)$  in the XY plane. This is implemented through [Algorithm 1](#), using moving least squares (MLS) [56] for calculation of the spatial-derivatives at the FEM nodes and FEM shape function for interpolation within a triangular element. It should be noted that a numerically expensive portion of the MLS method is the construction of the domain of dependence, which requires a search for the neighbouring nodes. In [Algorithm 1](#), MLS is used for evaluating spatial derivatives only at the FEM nodes. Hence the domain of dependence for each node can be constructed just once, before the time-stepping procedure, using the FEM linked-list. As a consequence, [Algorithm 1](#) requires minimum additional computational effort during the time-marching process. The MLS coefficients are calculated using linear polynomial basis function and bi-quadratic weight function. No additional filtering was applied on the high order spatial derivatives. It should be noted that the mesh size of

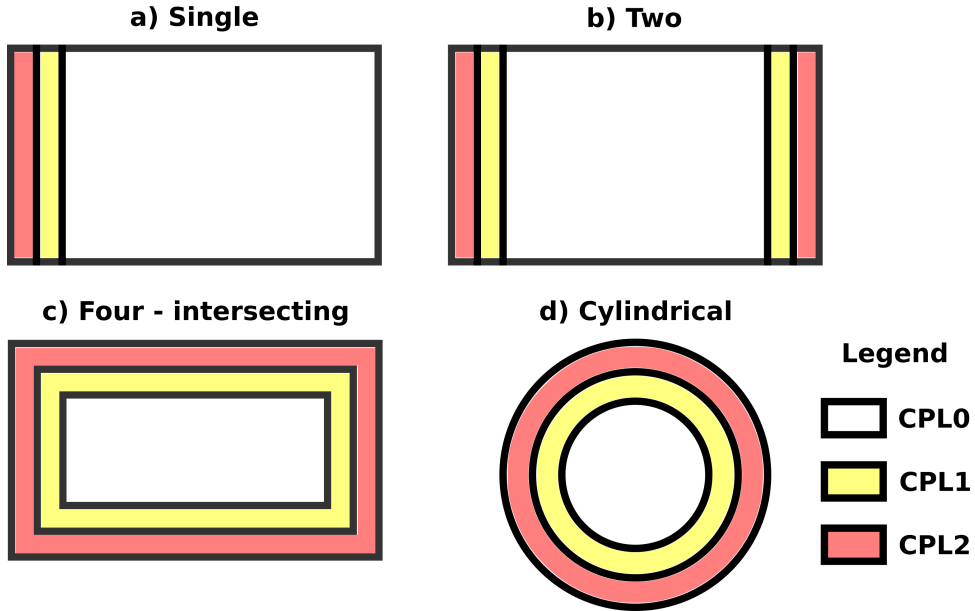


Figure 2: Top view of schematics showing various possible configurations of the coupling interface in the MLPG\_R domain. It also highlights the relative initial positions of the CPL0, CPL1 relaxation zone and CPL2 buffer zone nodes.

FEBOUSS will impact the coupling algorithm in two ways, 1) the solution of surface-elevation  $\eta$  and depth-integrated velocities ( $P, Q$ ) from the finite-element model, and 2) the vertical reconstruction of depth-resolved velocities ( $u, v, w$ ) and pressure  $p$  using [Algorithm 1](#).

The calculation of time-derivative in Eq. (10d) is carried out using three-point backward differencing method. Alternatively, the time-derivative can also be calculated using a central difference method. However, the latter would require calculation of FEBOUSS solution a few time-steps ahead of the MLPG\_R solution for the coupling procedure. As the differencing schemes are dependent on the size of the time-step, the time-derivative and hence the pressure will depend on the simulation time-step. The relative difficulty in accurately calculating the time-derivative is evident in the damped dynamic pressure for deeper waves in section 4.1. This is one of the key-reasons why the coupling procedure [Algorithm 2](#) was implemented without using pressure information.

#### *Algorithm 1.*

To compute depth-resolved quantities in FEBOUSS at an arbitrary point  $S(x, y, z)$

0. Values of  $P, Q, \eta$  known at time-step  $t_{n-1}$ .
1. Compute  $P, Q, \eta$  at time-step  $t_n$  using FEM and RK4 time-marching.
2. Calculate  $\nabla_h \bar{\mathbf{u}}$ ,  $\nabla_h(\nabla_h \cdot \bar{\mathbf{u}})$ ,  $\nabla_h \cdot \nabla_h(\nabla_h \cdot \bar{\mathbf{u}})$ ,  $\nabla_h \cdot \bar{\mathbf{u}} h$ ,  $\nabla_h(\nabla_h \cdot \bar{\mathbf{u}} h)$  and  $\nabla_h \cdot \nabla_h(\nabla_h \cdot \bar{\mathbf{u}} h)$  using MLS at all FEM nodes.
3. Find the triangle encompassing the  $(x, y)$  coordinates of point  $S$  using the method of cross-products.
4. Compute the values of derivatives of  $\bar{\mathbf{u}}$  at the  $(x, y)$  using the nodal values and FEM shape function of the encompassing triangle.
5. Compute  $u, v, w$  and  $p$  at point  $S(x, y, z)$  using Eq. (10).

#### *3.2. Coupling interface*

The discussion in the introduction section 1 is used for determining the appropriate coupling interface for one-way coupling of FEBOUSS with MLPG\_R. The flow in the coupling interface is assumed to be non-breaking and non-viscous. The depth-resolved velocities from FEBOUSS are determined using a perturbation-method based formula, which will have reduced consistency with the MLPG\_R velocities, especially for steeper waves. Further, as shown in section 4.1, the accuracy of depth-resolved pressure obtained from this method is poor, due to the requirement of the time-derivative. Therefore, we will only use the horizontal components of velocity for coupling. Additionally, the coupling in 3D may require various combinations of intersecting coupling interfaces as shown in Fig. (2). Here, the single coupling interface is primarily for wave-inlet into the MLPG\_R domain, while the two coupling interfaces can be used as inlet and outlet. The four intersecting or cylindrical coupling interfaces are ideal for truly 3D case, where they are encompassing the complete domain. The moving relaxation zone method provides the required flexibility for meeting the above-mentioned requirements. It can numerically ramp the solution between the two solvers and absorb the differences due to presence of structures in the MLPG\_R domain.

The nodes in MLPG\_R domain are classified into three categories, CPL0, CPL1 and CPL2, as shown in Fig. (2). The CPL0 nodes form the inner domain and are purely driven by the MLPG\_R solution. The CPL1 nodes form the relaxation zone region, which are driven by a combined solution,  $\Phi = C\Phi^F + (1 - C)\Phi^M$ . Here,  $\Phi^F$  and  $\Phi^M$  are the horizontal components of velocity  $u, v$  from FEBOUSS and MLPG.R respectively. The variable  $C$ , defined by Eq. (11), is the hyperbolic relaxation function from [32]. As per the conclusions in [32], the head of the relaxation function (region around to  $C = 1$ ) has a

larger contribution in wave-generation, while a long tail is necessary for wave-absorption. The parameters  $\alpha$  and  $\beta$  in Eq. (11) can hence be used for controlling the shape of  $C$  for efficient coupling. The variable  $x_r$  in Eq. (11) is the non-dimensional position of a point in the relaxation zone of width  $W_{RZ}$ . The value of  $x_r = 0$  indicates purely FEBOUSS and  $x_r = 1$  indicates purely MLPG\_R solutions. For intersecting relaxation zones, the  $x_r$  is calculated with respect to the closest boundary. We define the relaxation zone and  $C$  using the position of nodes at the zeroth time-step.

$$C(x_r, \alpha, \beta) = \frac{\tanh((x_r + \alpha)\beta) - \tanh((x_r - \alpha)\beta)}{\tanh(a\beta) - \tanh(-a\beta) - \tanh((1 + \alpha)\beta) + \tanh((1 - \alpha)\beta)} - \frac{\tanh((1 + \alpha)\beta) - \tanh((1 - \alpha)\beta)}{\tanh(a\beta) - \tanh(-a\beta) - \tanh((1 + \alpha)\beta) + \tanh((1 - \alpha)\beta)}$$

for  $x_r \in [0, 1]$

(11)

CPL2 nodes are buffer nodes, which serve the function of completing the domain of dependence [52] for the MLPG\_R solution of the CPL1 nodes. This procedure prevents partial sub-domains in the meshless solution. Their horizontal components of velocity  $u, v$  are driven purely by FEBOUSS solution, hence making them consistent with the CPL1 nodes having  $C = 1$ . However their vertical position is re-adjusted using the highly accurate surface elevation  $\eta$  solution from FEBOUSS. Similar to CPL1 nodes, these nodes are classified using their position at the zeroth time-step. Both the FEBOUSS and MLPG\_R models are solved using the same time-step  $\Delta t$ . Based on the results from [1] and [2], the MLPG\_R model will require a smaller spatial resolution ( $L/100$ ) compared to FEBOUSS ( $L/25$ ) for capturing the same wave-length  $L$ . Therefore, the time-step  $\Delta t$  for the coupled model will be limited by the stability condition for MLPG\_R. It will require a Courant number  $Cou \approx 0.5$  in the MLPG\_R sub-domain [2], resulting in  $Cou \approx 0.12$  in the FEBOUSS domain. The implementation of the coupling procedure is described in Algorithm 2.

#### Algorithm 2.

Implementation of coupling interface in MLPG\_R for input from FEBOUSS.

0. Solution of FEBOUSS and MLPG\_R at time-step  $t_{n-1}$  are known.
1. Compute the solution of FEBOUSS at time-step  $t_n$ .
2. Follow Algorithm 1 for computing depth-resolved velocity  $\vec{u}_n^F$  at  $t_n$  from FEBOUSS at all CPL1 and CPL2 node positions.
3. Compute intermediate velocity  $\vec{u}^*$  for MLPG\_R nodes using Eq. (5a).
4. Evaluate the pressure  $p_n$  at  $t_n$  by solving the pressure Poisson equation Eq. (6)
5. Calculate the velocity  $\vec{u}_n^M$  at  $t_n$  using Eq. (5b) for MLPG\_R nodes.

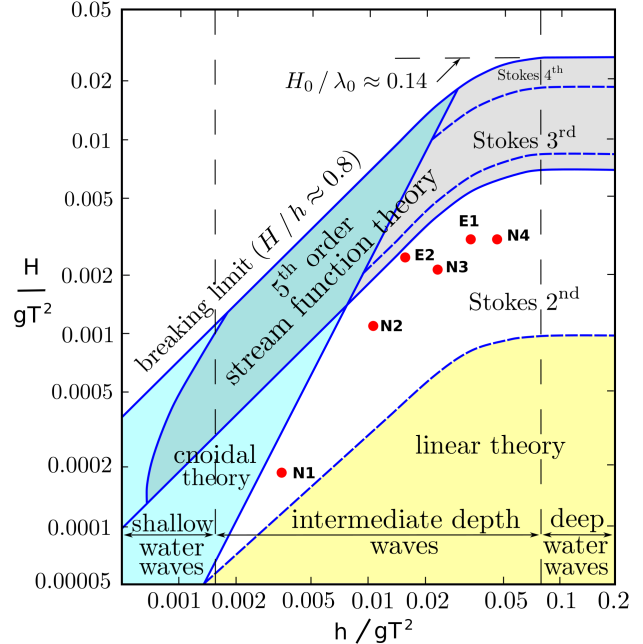


Figure 3: Plot adapted from [57] depicting the various regular wave cases tested in this manuscript. Here  $h/gT^2$  is the normalised water-depth and  $H/gT^2$  is the normalised wave-height. The original figure classifying the regions of validity for various theories is sourced from Wikimedia Commons [58], the free media repository.

6. For CPL1 nodes, use the relaxation function  $C$  to update only the horizontal components  $u, v$  of velocity using  $\Phi = C\Phi^F + (1 - C)\Phi^M$ , resulting in the final  $\vec{u}_n$ .
7. For CPL2 nodes, replace the horizontal components  $u, v$  of velocity using  $\Phi = \Phi^F$  to obtain the final  $\vec{u}_n$ .
8. Move the MLPG\_R nodes using  $\vec{u}_n$  to update their position for time-step  $t_n$ .
9. Rearrange the vertical position of CPL2 nodes using surface elevation  $\eta_n$  at  $t_n$  from FEBOUSS.

## 4. Numerical Results

The following sub-sections present a number of test cases for studying the calculation of depth-resolved velocities from the Boussinesq model. Following this, the FEBOUSS to MLPG\_R coupling algorithm is analysed in various configurations. The regular waves used in these tests are tabulated in Table 2 and their position in the wave-regime plot is shown in Fig. (3). Here  $h$  is the still-water depth,  $T$  is the wave-period,  $H$  is the wave-height,  $L$  is the wave-length,  $kh = 2\pi h/L$  is the dispersion parameter,  $ka = (2\pi/L)(H/2)$  is the non-linearity parameter,  $Ur = (HL^2)/h^3$  is the Ursell's parameter and finally  $h/gT^2$  and  $H/gT^2$  are the normalised water-depth and wave-height respectively. The presented manuscript will only study regular wave test cases to analyse the error in the calculation of depth-resolved velocity from FEBOUSS, and subsequently identify the associated impact on the MLPG\_R particle distribution within the coupling interface and the accuracy of the

Table 2: Table listing the specifics for each regular wave in the manuscript.

Name	<b>h</b> (m)	<b>T</b> (s)	<b>H</b> (m)	<b>L</b> (m)	<b>kh</b>	<b>ka</b> $10^{-2}$	<b>Ur</b> $\frac{L^2 H}{h^3}$	$\frac{h}{gT^2}$ $10^{-2}$	$\frac{H}{gT^2}$ $10^{-3}$
N1	0.50	4.00	0.03	8.6729	0.36	1.09	18.05	0.32	0.19
N2	1.00	3.00	0.10	8.6929	0.72	3.61	7.56	1.13	1.13
N3	1.00	2.00	0.08	5.2153	1.20	4.82	2.18	2.55	2.04
N4	1.00	1.50	0.06	3.3514	1.88	5.62	0.67	4.53	2.72
E1	0.86	1.50	0.06	3.2653	1.65	5.77	1.00	3.89	2.72
E2	0.70	2.00	0.10	4.6236	0.95	6.79	6.23	1.78	2.55

Table 3: Table listing regular mesh configuration used by FEBOUSS for simulation of regular waves in a rectangular tank with constant depth.

Name	<b><math>\Delta x</math></b> (m)	<b><math>\Delta t</math></b> (s)	<b><math>L/\Delta x</math></b>	<b><math>T/\Delta t</math></b>	<b>Cou</b> $\frac{\Delta t}{\Delta x} \sqrt{gh}$
N1	0.160	0.040	54.20	100	0.55
N2	0.160	0.030	54.33	100	0.59
N3	0.100	0.020	52.15	100	0.63
N4	0.050	0.010	67.03	150	0.62

hybrid solution against experimental, numerical and analytical references.

#### 4.1. Depth-resolved velocities from FEBOUSS compared against other models

In this section, we study the calculation of depth-resolved velocities from the FEBOUSS results using the [Algorithm 1](#). This exercise is required for identifying the appropriate variable for coupling and their accuracy for a range of waves. We use four regular wave cases ranging from  $kh = 0.3$  to  $kh = 2$  for covering shallow to intermediate depths. The details for these regular waves are listed as cases N1, N2, N3 and N4 in Table 2 and they belong to the Stokes-2<sup>nd</sup> order theory regime, as shown in Fig. (3). The case-N1 wave has three times the wave-height of the test case in [27], case-N2 is from [28] and case-N3 is from [29] (see Table 1). The comparison of FEBOUSS results will be done against the Stokes-2<sup>nd</sup> order theoretical results and numerical results from IITM-FNPT [59]. IITM-FNPT is a mixed Eulerian-Lagrangian finite element model for fully non-linear potential theory, which has been proven against a range of solitary, regular, focusing and long-wave cases.

The simulation of each test case in FEBOUSS is done using a rectangular domain with the specified constant depth  $h$ . The domain is meshed using regularly spaced nodes connected using right-angled triangles. For the test case with wave-length  $L$ , the FEBOUSS domain has a length of  $23L$ , width  $4h$ , with wave-making BC along the left boundary, slip walls along the side boundaries and a  $3L$  sponge layer at the right boundary. The

simulation is executed for  $25T$  duration for obtaining a steady state, where  $T$  is the wave-period. Measurements of surface-elevation and velocities were done at a distance of  $5.75L$  to  $6L$  from the wave-making boundary. Trials for mesh and time-step convergence were carried out similar to the work in [1]. However, the convergence trials are not presented in this manuscript for brevity. Converged results for each test-case were obtained using mesh-characteristics listed in Table 3. As per the conclusions of [1], a mesh size of  $L/25$  and  $T/50$  was sufficient to obtain converged results for the surface elevation of regular waves. However, owing to the high order derivatives involved in the calculation of depth-resolved velocities, a finer mesh resolution of  $L/55$  and time-step of  $T/100$  was required to obtain converged results for depth-resolved velocities for the majority of the presented cases.

Fig. (4) shows the comparison of surface elevation time-series for all for test-case. Here we can observe the nature of each test-case. Case-N1 is a shallower depth wave (low  $kh$ ) which is highly asymmetric about the mean-sea level (high  $Ur$ ). On the other hand case-N4 is a deeper wave (high  $kh$ ) with symmetry about the mean-sea level (low  $Ur$ ). With the error in FEBOUSS being proportional to products of dispersion and non-linearity parameters, these test-cases are well within the applicable range for this model. FEBOUSS results are observed to match well with the Stokes-2<sup>nd</sup> order theory and IITM-FNPT simulation for all four test cases, where it reproduces the required asymmetry in the wave-profile. The same can be observed in the comparison of depth-integrated velocity, shown in Fig. (5).

With the confirmation of the applicability of FEBOUSS for these cases, we now look into the [Algorithm 1](#) for calculating depth-resolved quantities. Fig. (6) shows the comparison of depth-resolved profiles for the horizontal  $u$  and vertical  $w$  components of velocity under the wave-crest. For the shallow-depth case-N1,  $u$  has a hyperbolic profile with low decay from crest to bottom. This profile is comfortably captured by the quadratic expression in Eq. (10a). The  $w$  profile for case-N1 is almost linear. We observe some variation in the peak value across the three results, however, the FEBOUSS result matches fairly well with IITM-FNPT. In the remaining case, with the increasing  $kh$ , we observe an increasing decay in  $u$  along the depth. Further,

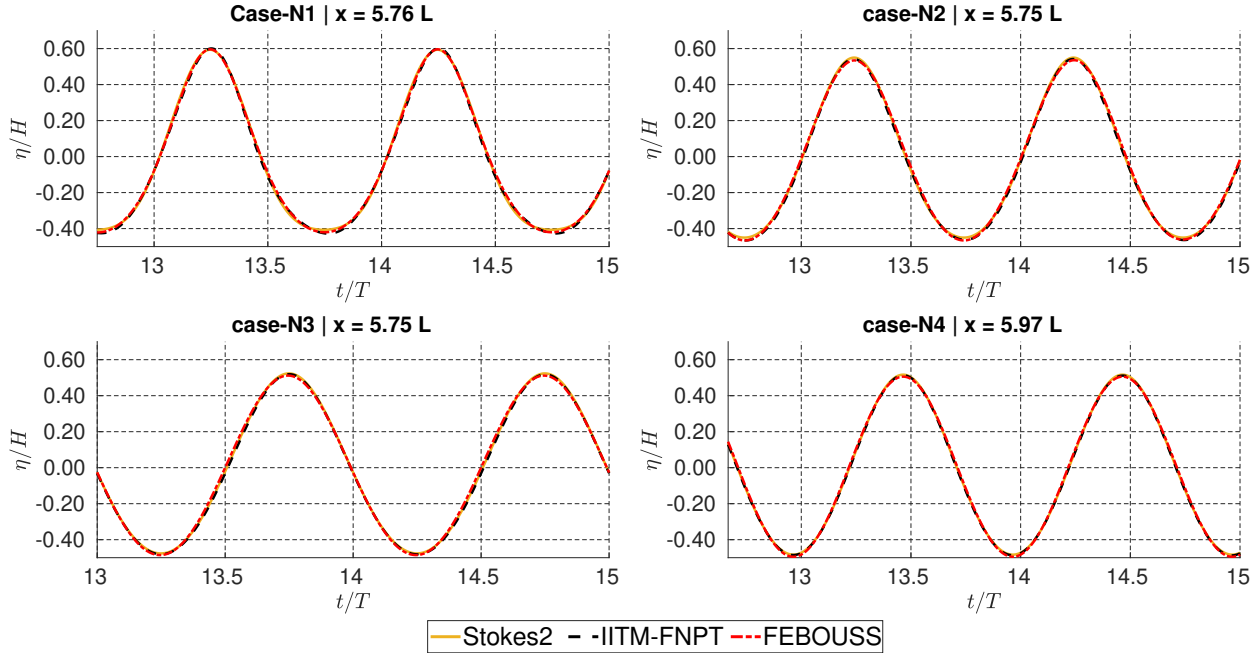


Figure 4: Comparison of surface-elevation  $\eta$  time-series obtained from FEBOUSS against Stokes-2<sup>nd</sup> order theory and IITM-FNPT [59] numerical results.

the profile for  $w$  too has an increasing curvature, progressing from linear to hyperbolic. The depth-profiles for cases N2 and N3 are fairly reproduced by FEBOUSS. However, for case-N4, FEBOUSS estimates a larger peak for  $u$  with a stronger decay along the depth. Finally, Fig. (7) shows the comparison for pressure time-series at a depth of  $z = -0.8h$ . We observe a good comparison for cases N1 and N2, a poor comparison in trough for case-N3 and highly damped dynamic pressure in case-N4. This damping is expected due to the requirement of the time-derivative of the gradient for pressure calculation as per Eq. (10d).

From these results, we can draw conclusions regarding the choice of variables for coupling with MLPG\_R. The surface-elevation and depth-integrated velocity are direct solutions from FEBOUSS, with accurate solutions till intermediate depths. The vertically reconstructed velocity and pressure are post-processed from FEBOUSS solution, introducing additional error from the assumptions in the derivation of Eq. (10) and the numerical calculation of derivatives. Among these variables, it is observed that depth-resolved horizontal components of velocity have reasonable accuracy up to  $kh = 2$ , while the depth-resolved pressure has a damped dynamic component for deeper waves, primarily due to the time-derivative. Therefore, the coupling will be carried out only using horizontal components of depth-resolved velocity ( $u, v$ ) and surface-elevation ( $\eta$ ).

The procedure for coupling described in section 3.2 is based on these conclusion. Here, the  $u$  and  $v$  components will be used for the CPL1 relaxation zone nodes, where the flow velocity will be adjusted as linear combination of FEBOUSS and MLPG\_R velocities using the relaxation function  $C$ . The CPL2 nodes are primarily present to complete the domain of dependence for the CPL1 nodes. Their positioning should be driven by the wave to ensure the continuity of particles. Therefore their

horizontal position will be driven by  $u$  and  $v$  from FEBOUSS, but their vertical position will be re-adjusted using  $\eta$ . The pressure from FEBOUSS is not used in the coupling procedure.

#### 4.2. Validation of depth-resolved velocities from FEBOUSS against experiment

The numerical calculation of depth-resolved velocities from FEBOUSS using the algorithm in section 3.1 is validated against experimental measurements from [60]. These measurements were a part of series of experiments performed by Delft Hydraulics Laboratory for propagation of regular waves over a submerged trapezoidal bar. The laboratory flume, as described in [60], was 45m long and 1m wide with a still-water depth of 0.86m. The trapezoidal bar had a slope of 1/20 towards the wave-maker and a slope of 1/10 towards the wave-absorber, with a minimum depth of 0.2m, as shown in Fig. (8). The measurement of flow velocity was done using a 3-beam 2-component laser Doppler velocimetry system (LDV) along various depths at  $x = 15.50\text{m}$  and  $x = 21.72\text{m}$  from the wave-maker.

The rectangular numerical domain is 60m long and 1m wide, with wave-maker BC along the left boundary, 10m long sponge layer along the right boundary and slip-wall BC along the side boundaries. The experiments were carried out for a wave with time-period  $T = 1.5\text{s}$  and wave-height  $H = 0.06\text{m}$ , resulting in a wave-length of  $L = 3.26\text{m}$  with  $kh = 1.65$  at the wave-maker. The specifics for the regular wave and its position in the wave-regime plot is shown with label E1 in Table 2 and Fig. (3) respectively. The domain is meshed using regularly spaced points connected by right-angled triangles. Following the procedures in [1], a converged result is obtained using  $\Delta x = \Delta y = 0.05\text{m} = L/65.30$  and  $\Delta t = 0.01\text{s} = T/150$ , with the maximum Courant number  $Cou = \Delta t \sqrt{gh}/\Delta x = 0.72$ .

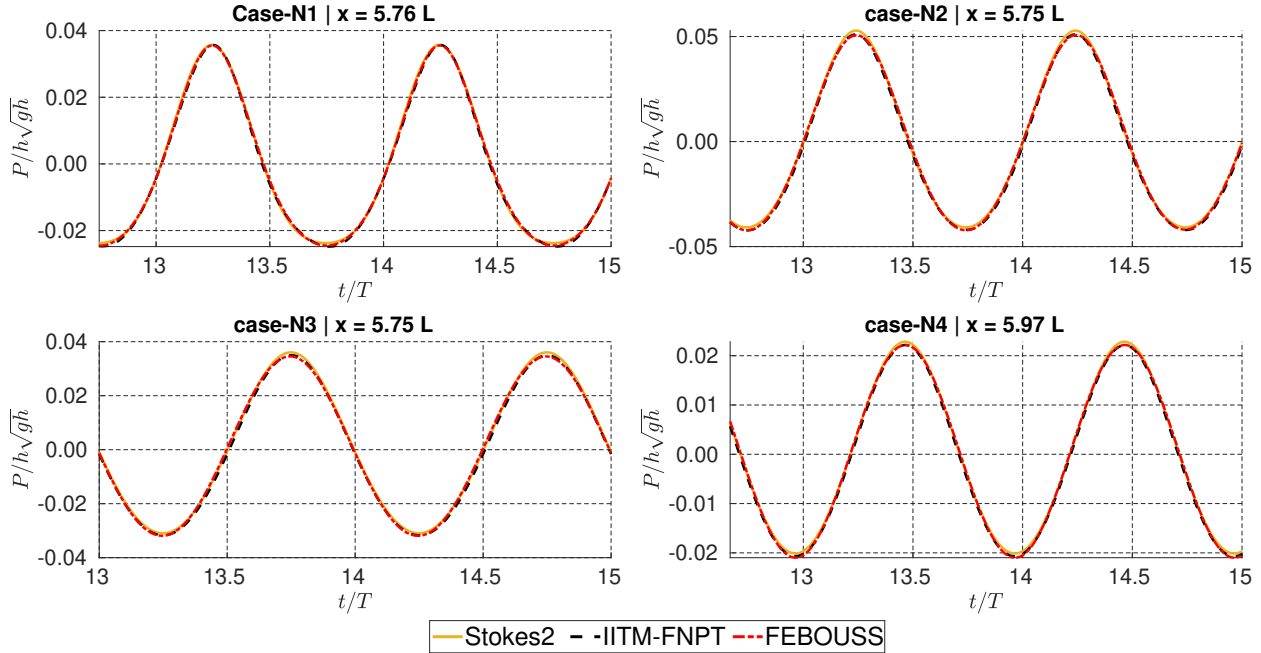


Figure 5: Comparison of depth-integrated velocity  $P$  time-series obtained from FEBOUSS against Stokes-2<sup>nd</sup> order theory and IITM-FNPT [59] numerical results.

The simulation was run for 60s and the comparison with experiments was carried out after achieving a steady-state.

Fig. (9) shows a comparison of the numerical results against the experimental measurements for surface-elevation  $\eta$  at four probes. The numerical model successfully replicated the increase in asymmetry about the mean-sea level with the decreasing depth along the shoal. However, a marginal overestimation of wave-crest near the top of the shoal can be noticed. Fig. (10) shows the depth-resolved profile of the horizontal velocity  $u$  under the wave-crest and wave-trough at locations  $x = 15.50\text{m}$  and  $x = 21.72\text{m}$ . Here the comparison is also carried out against numerical results from [54], in addition to the experimental results. The numerical model in [54] uses a 1D FDM model for weakly non-linear Boussinesq equation, with depth-resolved velocities calculated using Eq. (9). We observe a fair comparison between the experimental and FEBOUSS results. The profile for wave-trough matches well for both locations, and once again the peak velocity at wave-crest is over-estimated. It should be noted that [54] reported the requirement of smoothing the FDM solution for calculation of depth-resolved velocities. Whereas, no such additional smoothing was required by the results presented from FEBOUSS. Further, the FEBOUSS results show better agreement than [54] for all four plots in Fig. (10). This example thus demonstrates the reproduction of depth-resolved profile of velocity from FEBOUSS solution.

#### 4.3. Hybrid model: Single coupling interface

Numerical simulations were carried out using the hybrid model, where waves were transferred from the FEBOUSS domain to the MLPG\_R domain. In the first example, we transfer the regular wave defined by case-N2 (see Table 2), at a single coupling interface along the left face of the MLPG\_R do-

main as shown in Fig. (11). Here the FEBOUSS domain and mesh has the same specifics as mentioned in section 4.1. The 2D domain has a length of  $200.00\text{m} \approx 23L$ , width  $4h$ , with a prescribed still-water depth  $h$ , and is meshed using regularly spaced nodes at intervals of  $\Delta x = \Delta y = 0.16\text{m} = L/54.33$ , where  $L$  is the wave-length. It consists of wave-making BC along the left boundary, slip walls along the side boundaries and a  $3L$  sponge layer at the right boundary.

The MLPG\_R sub-domain is positioned within the FEBOUSS domain with its left corner initially at  $(x, y) = (39.80\text{m}, 1.75\text{m})$  as shown in Fig. (11). The MLPG\_R domain has a length of  $70.20\text{m}$ , width  $0.50\text{m}$  and initial depth of  $h = 1.00\text{m}$ , with the free-surface initially at  $z = 0\text{m}$  and bottom boundary at  $z = -1\text{m}$ . A detailed convergence analysis for modelling wave-structure interaction using MLPG\_R for regular and focusing waves was carried out in [2]. Following the procedures and conclusions of [2], converged results were obtained using regularly spaced particles initially placed at an interval of  $\Delta x = \Delta y = \Delta z = 0.05\text{m} = h/20$ . The 3D domain is bound by free-surface on the top and slip walls along the side-boundaries and bottom boundary, and a sponge layer of length  $3L$  at the right face. The coupling interface is placed along the left face of the domain. The coupling interface consists of two types of nodes, CPL1 nodes of the relaxation zone and the CPL2 of the buffer zone, as described in section 3.2. They are defined using their position at the zeroth time-step. The CPL2 nodes are located within a region of length  $L_{C2}$  adjacent to the left face, while the CPL1 nodes are in a region of length  $L_{C1}$  as shown in Fig. (11).

The CPL2 nodes serve the function of completing the integration sub-domain for the CPL1 nodes. Therefore 4 layers of these nodes was found to be sufficient, thus fixing  $L_{C2} = 4\Delta x = 0.20\text{m}$ . We tested various lengths  $L_{C1}$  of the relaxation

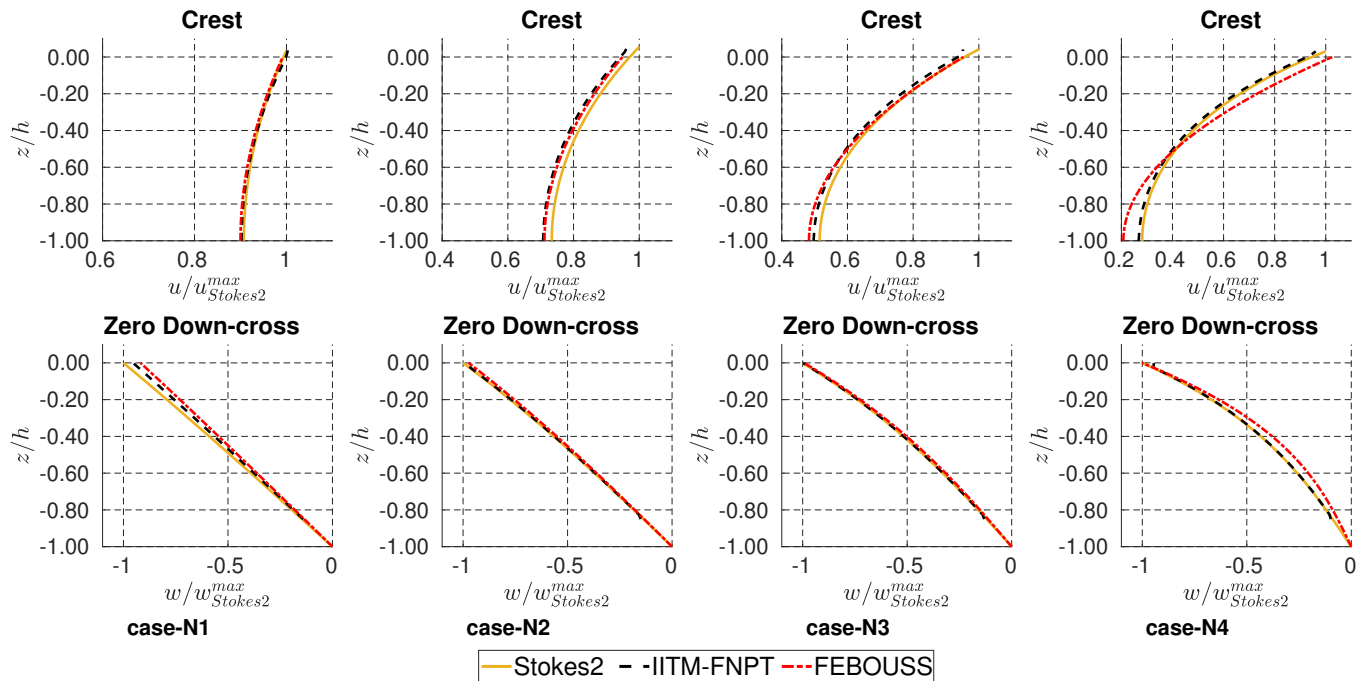


Figure 6: Comparison of depth-resolved profiles of  $u$  and  $w$  components of velocity vector obtained from FEBOUSS, against Stokes- $2^{nd}$  order theory and IITM-FNPT [59] numerical results. The velocity results are scaled against the maximum of Stokes- $2^{nd}$  order theory results for horizontal component under crest  $u_{Stokes2}^{max}$  and vertical components under zero down-crossing  $w_{Stokes2}^{max}$ .

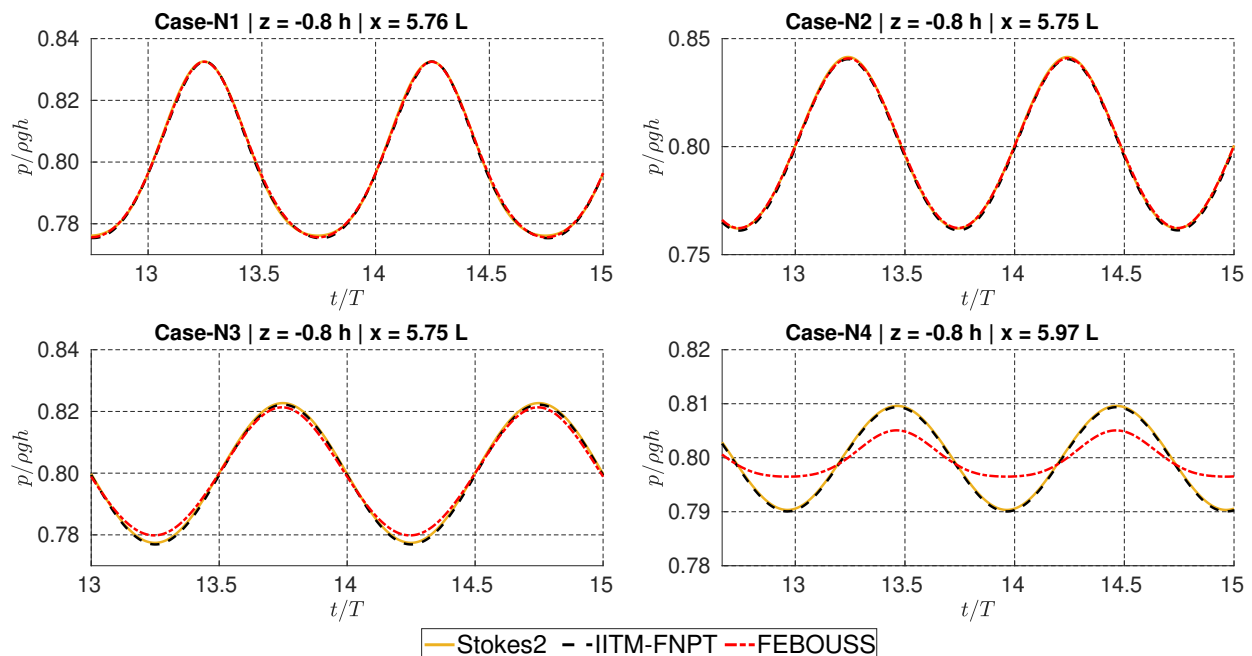


Figure 7: Comparison of pressure  $p$  time-series obtained from FEBOUSS against Stokes- $2^{nd}$  order theory and IITM-FNPT [59] numerical results at a depth of  $z = -0.5h$ .

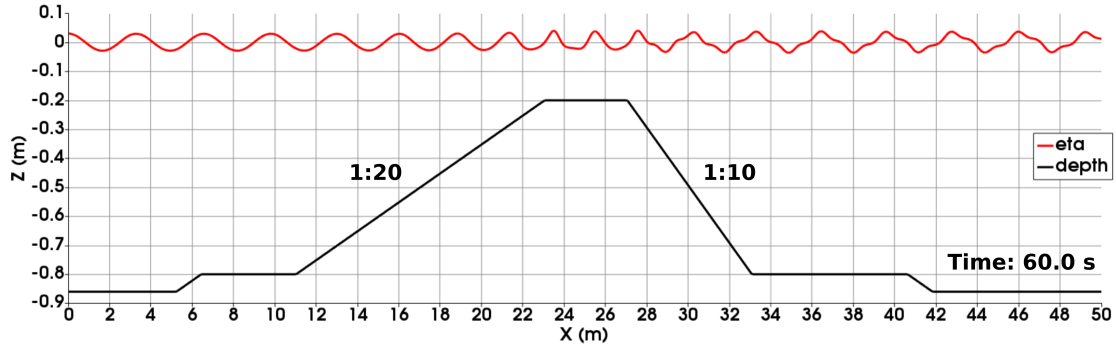


Figure 8: Plots for the depth-profile from [60] and evolution of the surface elevation  $\eta$  as it passes over the submerged trapezoidal bar.

zone for identifying its influence on the hybrid solution. The tests were done for  $L_{C1} \in [1.00\text{m}, 4.00\text{m}]$  corresponding to  $L_{C1}/L \in [0.12, 0.46]$ , where  $L$  is the wave-length. Hence in the coupled simulation, at zeroth time-step, the MLPG\_R domain starts from  $x = 39.80\text{m}$ , with the buffer layer CPL2 nodes in  $x \in [39.80\text{m}, 40.00\text{m}]$  and the relaxation zone CPL1 nodes  $x \in [40.00\text{m}, 40.00\text{m}+L_{C1}]$ . The relaxation function  $C$  given by Eq. (11) is defined using coefficient  $\alpha = 0.29, \beta = 5.0$ . This results in a relaxation function with long tail section (near  $C = 0$ ), which is ideal for absorbing any reflected waves as per the conclusions in [32]. The hybrid model is executed at the time-step of  $\Delta t = 0.008\text{s}$ , resulting in a Courant number of  $Cou = 0.15$  in the FEBOUSS region and  $Cou = 0.50$  in the MLPG\_R region.

The waves produced by the hybrid model in the MLPG\_R sub-domain are compared against the results from purely FEBOUSS and purely MLPG\_R simulations. The purely MLPG\_R simulation was done using the same node distribution and domain characteristics as the MLPG\_R sub-domain of the coupled simulation, except with the domain starting from  $x = 0.00\text{m}$  instead of  $x = 39.80\text{m}$ . The purely MLPG\_R domain has a total length of 110m, with the a wave-maker on the left face instead of a coupling interface. Comparisons were done for wave elevation  $\eta$  at a probe at  $(x, y) = (50.00\text{m}, 2.00\text{m})$  obtained from each model. The difference between wave-elevation time-series obtained from the hybrid model  $\eta_H$  and purely FEBOUSS simulation  $\eta_F$  for a long duration is quantified using relative amplitude parameter  $A_{r,HF}$  and phase difference parameter  $P_{d,HF}$  defined as follows, similar to the work in [30]. These values of  $A_r$  and  $P_d$  allow us to monitor the influence of changes in  $L_{C1}$ , and further compare single coupling interface against multiple coupling interfaces. The values of  $A_r \rightarrow 1$  and  $P_d \rightarrow 0$  indicates perfect agreement between two time-series.

$$A_{r,HF} = \sqrt{\frac{\sum_t (\eta_H)^2}{\sum_t (\eta_F)^2}}, \quad P_{d,HF} = \sqrt{\frac{\sum_t (\eta_H - \eta_F)^2}{\sum_t (\eta_F)^2}} \quad (12)$$

Further a comparison of the crest elevation values relative to purely MLPG\_R simulation was quantified using error parameter  $E_{HM,C}^\eta = \frac{|\eta_{H,C} - \eta_{M,C}|}{|\eta_{M,C}|} \times 100$  and  $E_{FM,C}^\eta = \frac{|\eta_{F,C} - \eta_{M,C}|}{|\eta_{M,C}|} \times 100$ , where  $\eta_{H,C}$ ,  $\eta_{F,C}$  and  $\eta_{M,C}$  are crest values from the hybrid, FEBOUSS and purely MLPG\_R simulations, respectively. The same procedure was repeated for the wave-trough. The value of

horizontal component  $u$  of velocity was measured at multiple probes along the depth at  $(x, y) = (50.00\text{m}, 2.00\text{m})$ . This provided us with the depth-resolved profile of  $u$  from each model at the same location. The comparison of these values under the wave-crest was quantified against purely MLPG\_R solution using error parameters  $E_{HM,C}^u$  and  $E_{FM,C}^u$ .

$$\begin{aligned} E_{HM,C}^u &= \sqrt{\frac{\sum_z (u_{H,C} - u_{M,C})^2}{\sum_z u_{M,C}^2}} \times 100, \\ E_{FM,C}^u &= \sqrt{\frac{\sum_z (u_{F,C} - u_{M,C})^2}{\sum_z u_{M,C}^2}} \times 100 \end{aligned} \quad (13)$$

Here  $u_{H,C}$ ,  $u_{F,C}$  and  $u_{M,C}$  are values of  $u$  from the hybrid, FEBOUSS and MLPG\_R simulations, respectively. This procedure was also repeated for wave-trough. Through these values of  $E^\eta$  and  $E^u$ , we can quantify the difference between purely FEBOUSS and MLPG\_R simulations, and further understand its impact on the hybrid solution.

Fig. (12a) shows the comparison of the surface elevation time-series obtained from the hybrid model using single coupling interface of  $L_{C1} = 1.50\text{m} = 0.17L$ , against the purely FEBOUSS simulation. This test case is labelled as L1.50R0.00 across the results. This comparison highlights the difference between the desired result from the FEBOUSS simulation and the obtained result from the hybrid simulation in the MLPG\_R sub-domain with FEBOUSS input. The figure indicates good agreement in phase, with marginal positive error in wave-crest and wave-trough. This is further confirmed by a low  $P_{d,HF} = 0.0578$  and marginal higher than 1 value of  $A_{r,HF} = 1.0075$ . This test was repeated for various  $L_{C1}$ , with the values of  $A_r$  and  $P_d$  plotted in Figs. (13a) and (13b), respectively. We can observe that the values of  $L_{C1}$  in the tested range have a very limited influence on the accuracy of the result. However,  $L_{C1}$  was found to have an impact on the distribution of the nodes in the relaxation zone within the MLPG\_R sub-domain. It should be noted that the relaxation function  $C$  given by Eq. (11) has dependence of  $\nabla \cdot C \propto 1/L_{C1}$ . Further, as discussed in the introduction section 1, the flow within the relaxation zone will have non-zero divergence, with  $\nabla \cdot \vec{u} = \nabla C \cdot (\vec{u}^A - \vec{u}^B)$ , and hence  $\nabla \cdot \vec{u} \propto 1/L_{C1}$ . If the two models being coupled have excellent agreement between their velocities, then the value of  $\nabla \cdot \vec{u}$  within the relaxation zone will be small, irrespective of  $\nabla C$ .

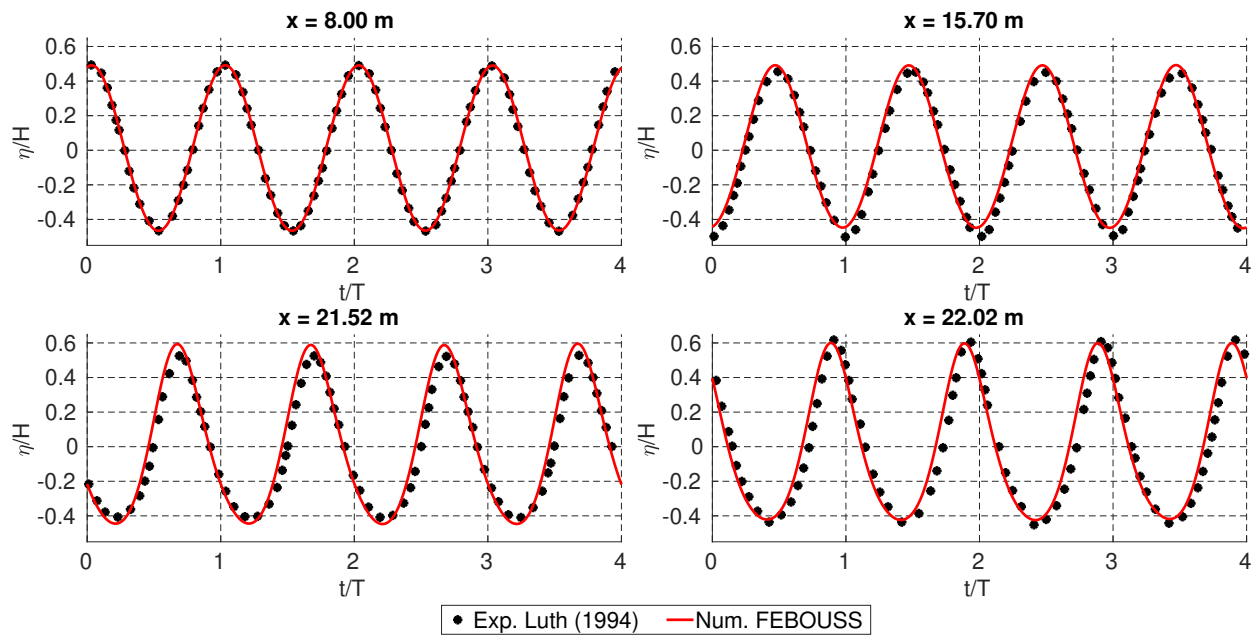


Figure 9: Plots showing the comparison of surface-elevation  $\eta$  between the experimental measurements of [60] and converged numerical results of FEBOUSS.

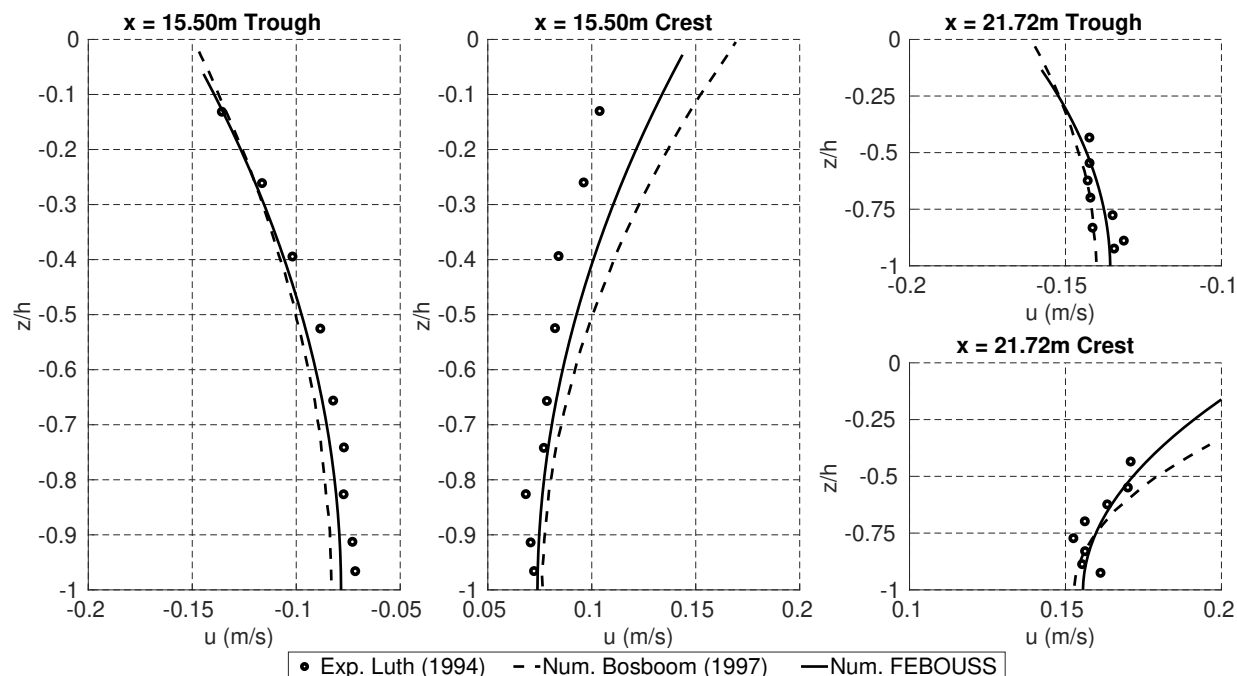


Figure 10: Plots for the depth-resolved profile of horizontal component  $u$  of velocity obtained from experimental measurements of [60] and numerical simulations of [54] and FEBOUSS.

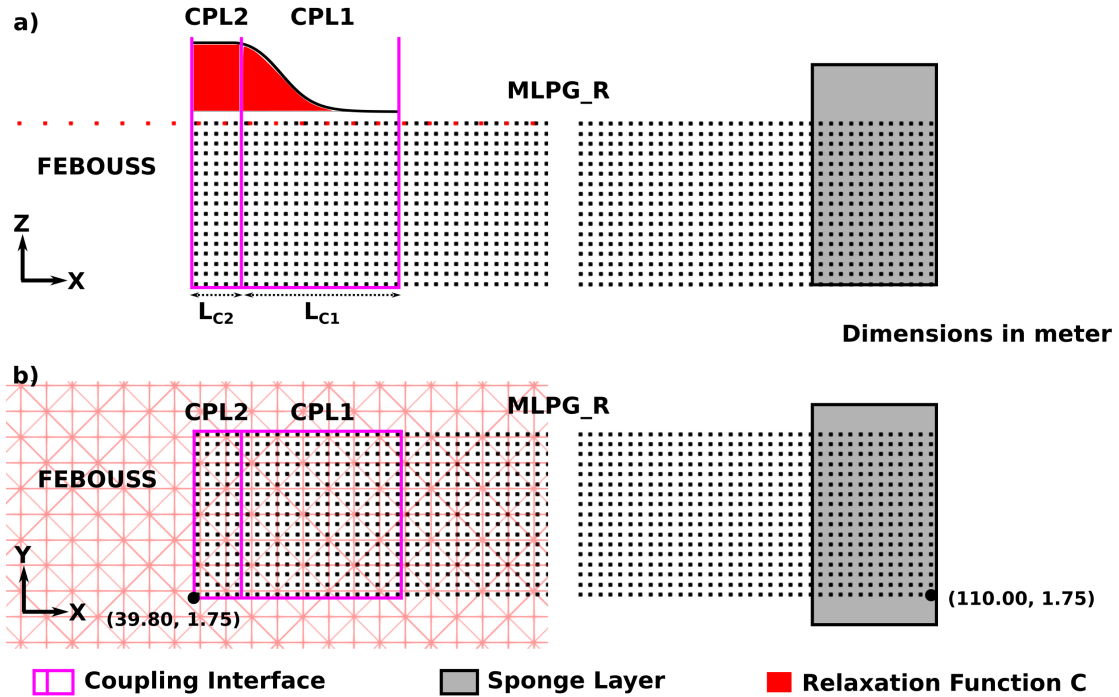


Figure 11: Schematics showing the arrangement of the FEBOUSS domain and the MLPG\_R domain near the single coupling interface. The schematics also show the regions defining the relaxation zone CPL1 nodes and buffer zone CPL2 nodes. a) The side-view of the domain, additionally depicting the relaxation function  $C$  defined by Eq. (11) with  $\alpha = 0.29, \beta = 5.0$  within the relaxation zone. b) The top-view of the domain.

For example, consider the coupling between IITM-FNPT and MLPG\_R in [2] (see Table 1). However, in the presented hybrid model, the fully resolved meshless MLPG\_R model and depth-integrated meshed FEBOUSS have significant differences in their characteristics. Therefore, a smaller  $L_{C1}$  will lead to larger disturbance in particle distribution within the relaxation zone, with a progressive concentration of the particles near the free-surface over long duration. In the presented test case, no numerical instability due to concentration of particles was observed for 10,000 time-steps using  $L_{C1} = 1.50\text{m} = 0.17L$ . It should be noted that this numerical artefact within the relaxation zone can be treated with periodic re-distribution of nodes without significant impact on accuracy.

Following the study on  $L_{C1}$ , the results from L1.50R0.00 are further scrutinised against purely MLPG\_R results. Fig. (14a) shows the comparison of wave-elevation  $\eta$  between the three results, with zoomed-in views of the crest and the trough shown in Figs. (14b) and (14c), respectively. The comparison of depth-resolved profile of the horizontal velocity component  $u$  under the wave-crest and trough is shown in Figs. (15a) and (15b), respectively. Further, the wave elevation at crest and trough from each model is tabulated in Table 4 with label L1.50R0.00, along with the relative error in wave elevation and velocity profile measured with respect to the purely MLPG\_R simulation.

We observe that both crest and trough from FEBOUSS are lower by about 2.50% compared to the purely MLPG\_R result. This implies that both the models produce nearly the same wave-height, with mid-elevation in FEBOUSS lower than MLPG\_R. Further, the difference in the  $u$  profile between the two models is only marginal 0.60% under the wave-crest, while

the profile under the wave-trough has larger deviation of 0.99% owing to difference in its shape. These differences between FEBOUSS and MLPG\_R are numerically smoothed by the relaxation zone. The elevation obtained from the resultant hybrid model has a 3.92% higher wave-crest and 3.13% higher wave trough compared to the MLPG\_R solution. Thus, the hybrid result produces nearly the same wave-height as purely MLPG\_R results, with marginally higher mid-elevation. The depth-profile of  $u$  in the hybrid model is similar to the MLPG\_R results. However, we can observe a positive drift in the values for both crest and trough by about 2.49% and 1.32%, respectively. It should be noted that the velocity profile obtained from the hybrid model does not have additional noise, unlike the results from [29] on 2D coupling of OceanWave3D and DualSPHysics (see Table 1). This is primarily due to the difference in the coupling method, where the work in [29] uses the changes in local particle density for generation waves in DualSPHysics from OceanWave3D input, unlike the relaxation zone approach in the presented model. Through this example, we have demonstrated the ability of the presented hybrid model to reproduce Stokes- $2^{nd}$  order regular wave within an acceptable error range using a single coupling interface.

#### 4.4. Hybrid model: Two coupling interfaces

The use of single coupling interface is a relatively common practice, where the exchange of variables between the two models happens only in a single zone. In these cases, the incoming waves are either absorbed by a sponge layer [2, 32, 61], or they are reflected by a wall / beach [27, 30]. The use of the sponge layer will lead to a longer Navier-Stokes domain. On the other

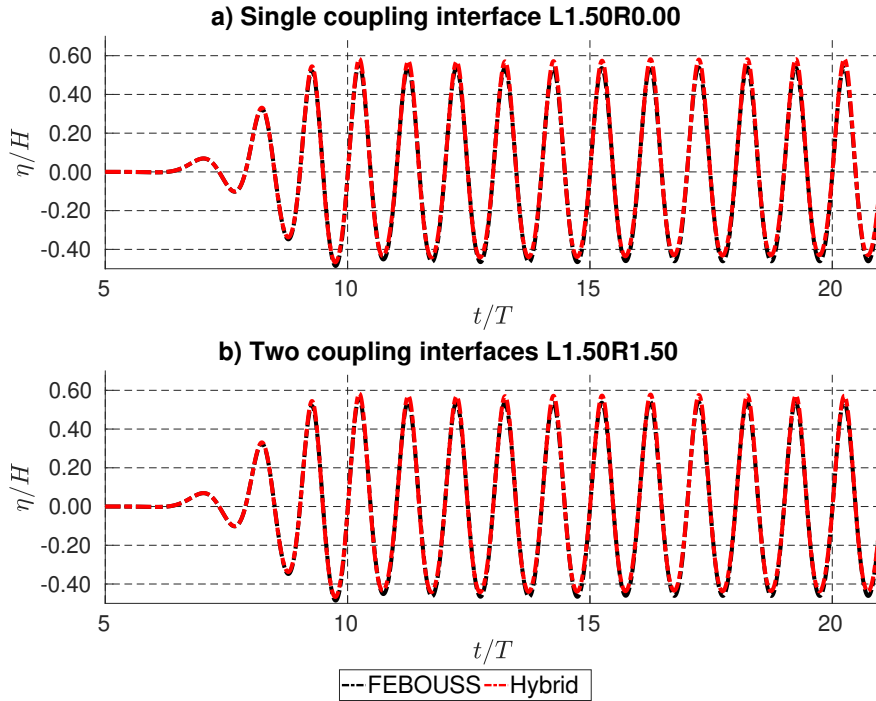


Figure 12: Plots showing comparison of surface-elevation  $\eta$  time-series obtained from the hybrid model simulations and FEBOUSS simulation, at a probe located at  $(x, y) = (50\text{m}, 2\text{m})$ . a) Results from hybrid model with single coupling interface. b) Results from hybrid model with two coupling interfaces.

hand, the walls / beach condition may only be limited to run-up studies. In order to expose structures to consistent waves over long duration in a hybrid model, it is crucial to enable the exchange of variables at multiple locations through multiple coupling interfaces.

Therefore, following our investigation with the single coupling interface, we now use two coupling interfaces in the MLPG\_R domain of the hybrid model, one along the left face and one along the right face. This method will enable both the generation and absorption of waves in the MLPG\_R sub-domain, using the input from FEBOUSS simulation at both the coupling interfaces.

Similar to the single interface tests, the two coupling interface numerical tests are carried out for the regular wave case-N2 (see Table 2). The simulation setup is depicted in Fig. (16). The FEBOUSS domain has the same specifics as the previous example. The MLPG\_R domain now has a length of 35.20m, width 0.5m, initial depth of  $h = 1\text{m}$  with particles placed at regular interval at initial spacing of  $\Delta x = \Delta y = \Delta z = 0.05\text{m} = h/20$ . It is bound by slip wall BC along the side and bottom walls, the free-surface on the top and coupling interfaces along the left and the right faces. This MLPG\_R sub-domain is positioned within the FEBOUSS domain with its left corner at  $(x, y) = (39.80\text{m}, 0.75\text{m})$  as shown in Fig. (16). Once again, four layers of buffer zone CPL2 nodes are set along the left and the right faces, with  $L_{C2} = 4\Delta x = 0.20\text{m}$ . We tested various lengths of the relaxation zone  $L_{C1}$  to investigate its influence on the results. Therefore, at zeroth time-step, the MLPG\_R domain is located in  $x \in [39.80\text{m}, 75.00\text{m}]$ , with the buffer zone CPL2 nodes in  $x \in [39.80\text{m}, 40.00\text{m}] \cup [74.80\text{m}, 75.00\text{m}]$  and the

relaxation zone CPL1 nodes in  $x \in [40.00\text{m}, 40.00\text{m} + L_{C1}] \cup [74.80\text{m} - L_{C1}, 74.80\text{m}]$ . Hence, the initial distance between the start of the both relaxation zones is  $34.80\text{m} \approx 4L$ . The hybrid model is executed at a constant time-step of  $\Delta t = 0.008\text{s}$ , corresponding to Courant number  $Cou = 0.15$  in the FEBOUSS domain and  $Cou = 0.50$  in the MLPG\_R domain. Similar to section 4.3, the relaxation function  $C$  is once again defined using  $\alpha = 0.29, \beta = 5.0$  resulting in a crucial long-tail portion.

Fig. (12b) shows resultant  $\eta$  time-series from the MLPG\_R sub-domain of the hybrid model, having two coupling interfaces each with  $L_{C1} = 1.50\text{m} = 0.17L$ , labelled as L1.50R1.50. It is compared against purely FEBOUSS simulation. For this case, the value of relative amplitude  $A_{r,HF} = 1.0070$  is similar to the L1.50R0.00 result. The same is observed for all test cases with  $L_{C1} \in [0.50\text{m}, 4.50\text{m}] \equiv L_{C1}/L \in [0.06, 0.79]$ , as shown in Fig. (13a), where  $A_{r,HF}$  is similar for both single and two coupling interfaces. Further, the comparison of wave-crest and trough values from the hybrid model L1.50R1.50 against the MLPG\_R values yields error of  $E_{HM,C}^\eta = 3.88\%$  and  $E_{HM,T}^\eta = 3.08\%$ , similar to L1.50R0.00 results, as tabulated in Table 4.

However the phase difference in L1.50R1.50 corresponds to  $P_{d,HF} = 0.0520$ , which is 10% lower than the L1.50R0.00. Similar observation is made across  $L_{C1}/L$  values as shown in Fig. (13b). A wave simulated by MLPG\_R and FEBOUSS will have marginally different phase speeds. In case of single coupling interface, this marginal difference is smoothed only at the inlet, while in the case of two coupling interfaces, this difference is corrected at the inlet and outlet, resulting in lower phase difference with respect to FEBOUSS result. Over-

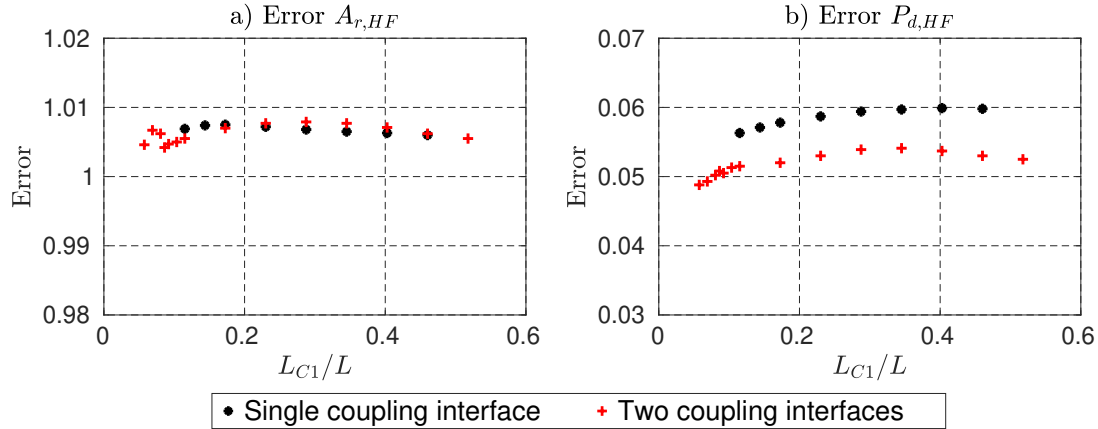


Figure 13: Plots reporting relative error in the surface-elevation  $\eta$  time-series at  $(x, y) = (50\text{m}, 2\text{m})$  obtained from hybrid model simulations with respect to FEBOUSS simulation results. a) Plot of relative amplitude parameter  $A_{r,HF}$  from both single and two coupling interfaces. b) Plot of phase difference parameter  $P_{d,HF}$  from both single and two coupling interfaces.

all, we still observe a limited influence of  $L_{C1}$  on the accuracy of the hybrid model result. Further, observations regarding its influence on the particle concentration within the relaxation zone are similar to the remarks from single coupling interface. Finally, the  $u$  profile from L1.50R1.50 too is quite similar to the L1.50R0.00 result, with the error of  $E_{HM,C}^u = 2.59\%$  and  $E_{HM,T}^\eta = 1.34\%$  under wave-crest and trough, respectively. The plot of depth-resolved profile of velocities obtained from L1.50R1.50 is nearly identical to the result obtained from L1.50R0.00. Hence, it is not reported again.

Through these tests we have demonstrated the ability to generate waves in MLPG\_R domain using input from FEBOUSS with acceptable error to create a hybrid model. On the other hand, the run-time gains from the hybrid approach are significant due to the reduction of the MLPG\_R domain size and relatively low numerical cost of FEBOUSS. Fig. (17) contrasts the relative size of MLPG\_R domain for simulation with no coupling against the hybrid model with single and two coupling interfaces. Further, the Table 5 lists the wall-clock time taken by the simulations for modelling the same wave from still-water to 7500 time-steps. Each simulation was executed on a Intel(R) Xeon(R) Gold 2.50GHz CPU with 8 cores and parallel implementation using OpenMP. We observe that the hybrid simulation with single (L1.50R0.00) and two (L1.50R1.50) coupling interfaces takes 71.21% and 35.25% of the original run-time, respectively. The gain is primarily due to the drastic reduction of the MLPG\_R domain to 63.82% and 32.00% of its original length in L1.50R0.00 and L1.50R1.50, respectively. The time taken by FEBOUSS is nearly the same (0.9h) for both the hybrid simulation because there is no difference in its setup. Table 5 also presents the total time taken by the coupling algorithm, including the calculation of spatial derivatives and depth-resolved quantities in FEBOUSS, and the interpolation to the moving MLPG\_R nodes in the coupling zone. The coupling time for two coupling interfaces (0.06h) is twice the time taken for single coupling interface (0.03h). However, crucially the time taken by coupling is marginal for both the hybrid simulations, highlighting the efficiency of the algorithms and imple-

mentation. This hybrid model thus has the potential to enable the simulation of large domain real-world problems using particle based methods.

#### 4.5. Hybrid model: 3D coupling

Both FEBOUSS and MLPG\_R have been developed for simulating waves in three-dimensional domain. Further, the Algorithm 1 and Eq. (10) provide all three components of velocity  $\vec{u} = \hat{u}\hat{i} + \hat{v}\hat{j} + \hat{w}\hat{k}$  using the results from Boussinesq equation. Therefore, in the present section, we demonstrate the ability of Algorithm 2 for coupling the two models in 3D using a directional wave test case. We continue to test using the regular wave defined by case-N2 (see Table 2). However, for this section the wave-direction is prescribed as  $30^\circ$  with respect to the X-axis, unlike the previous section where the wave-direction was prescribed along the X-axis.

The directional wave test case is carried out for 1) investigating calculation of the derivatives and cross derivatives of  $P$  and  $Q$  during calculation of the depth-resolved quantities using Eq. (10), 2) monitoring the MLPG\_R particle distribution within the relaxation zone, 3) presenting first demonstration of directional-wave using this type of hybrid model. Appendix A presents an example, where the issue with particle distribution near the intersection of coupling interfaces was only evident in case of directional test-case.

The FEBOUSS domain is a rectangular wave tank of length  $200\text{m} \approx 23L$  and width  $16\text{m}$ , which is rotated anti-clockwise by  $30^\circ$  about the Z-axis, as shown in Fig. (18a). This allows us to consistently generate regular waves at  $30^\circ$  in the FEBOUSS domain. It is bound by side DA with wave-making boundary condition, sides AB and CD with slip-wall boundary condition, and a sponge layer of length  $3L$  next the side BC. The domain has a constant still-water depth of  $h = 1.0\text{m}$ . The domain is meshed using nodes placed at regular interval of  $0.16\text{m} \approx L/54.33$ , connected using right-angled triangles, similar to the previous sections.

The MLPG\_R sub-domain is a cylinder with its axis parallel to the Z-axis. This shape allows for wave-input into the

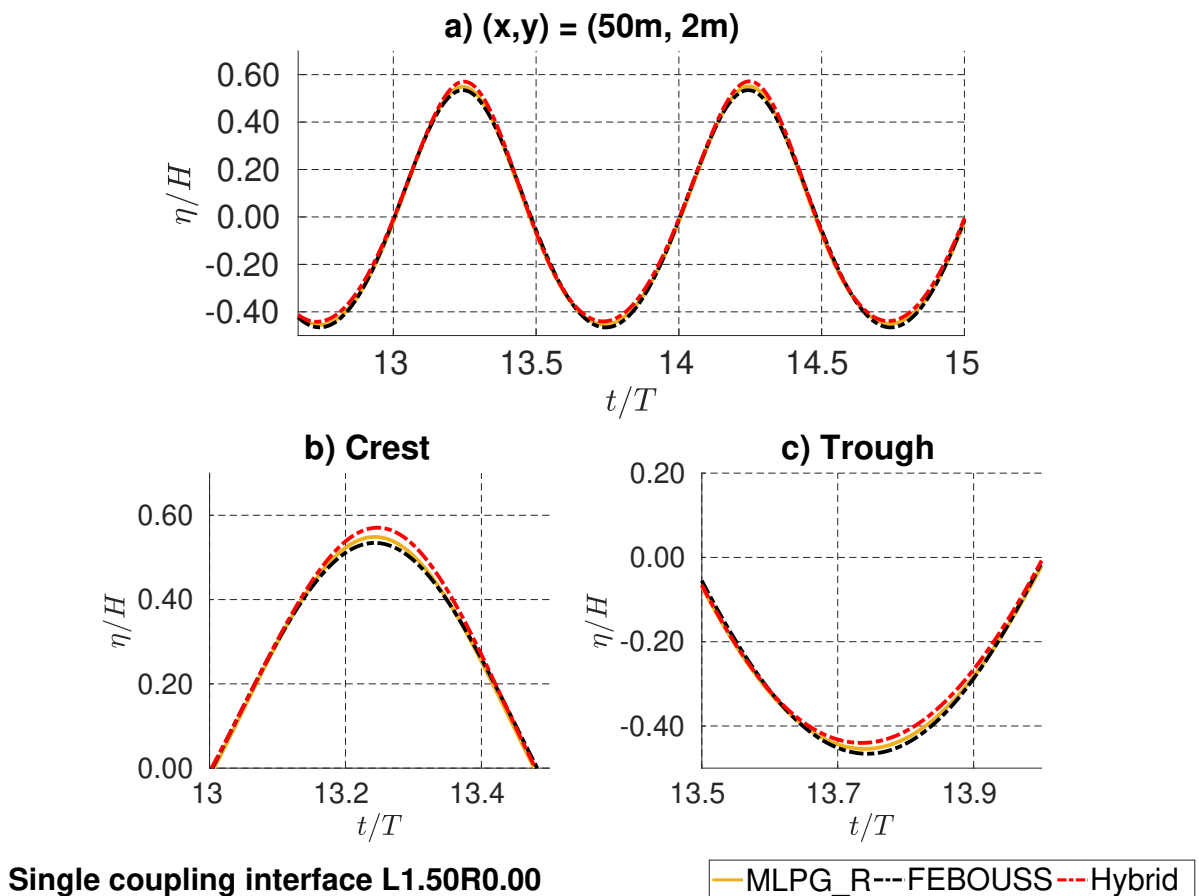


Figure 14: Figures showing comparison of results from purely MLPG\_R, purely FEBOUSS and the hybrid model. a) Comparison of wave elevation at  $(x,y) = (50\text{m}, 2\text{m})$  b) Wave-elevation comparison with zoomed in view of the wave-crest. c) Wave-elevation comparison with zoomed in view of the wave-trough. Here  $H$  is the specified wave-height and  $T$  is the wave-period.

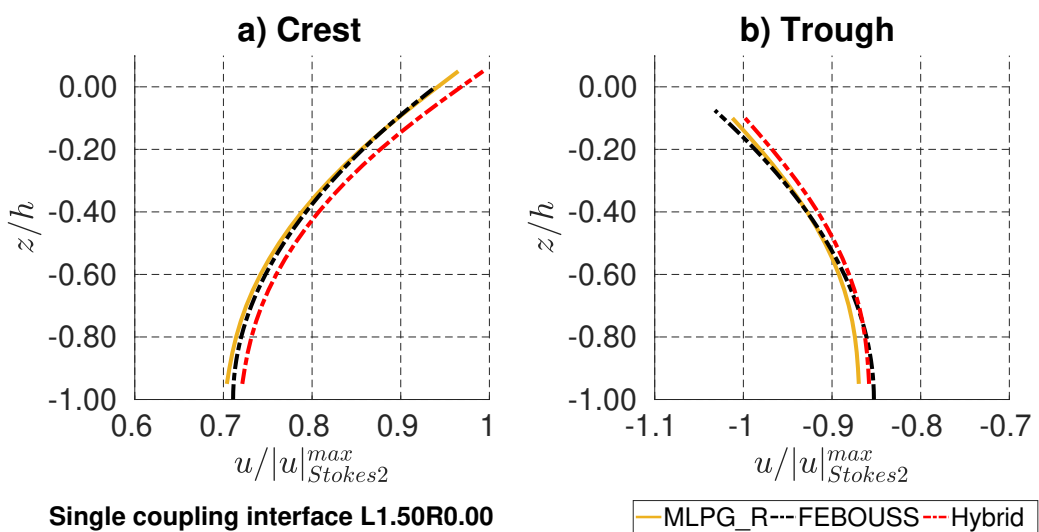


Figure 15: Figures showing comparison of results from purely MLPG\_R, purely FEBOUSS and the hybrid model for depth-resolved profile of horizontal component  $u$  of velocity under a) wave-crest, b) wave-trough. Here  $h$  is the still-water depth. The velocity is non-dimensionalised using the absolute value of peak velocity from Stokes-2<sup>nd</sup> order theory under the crest and trough, respectively.

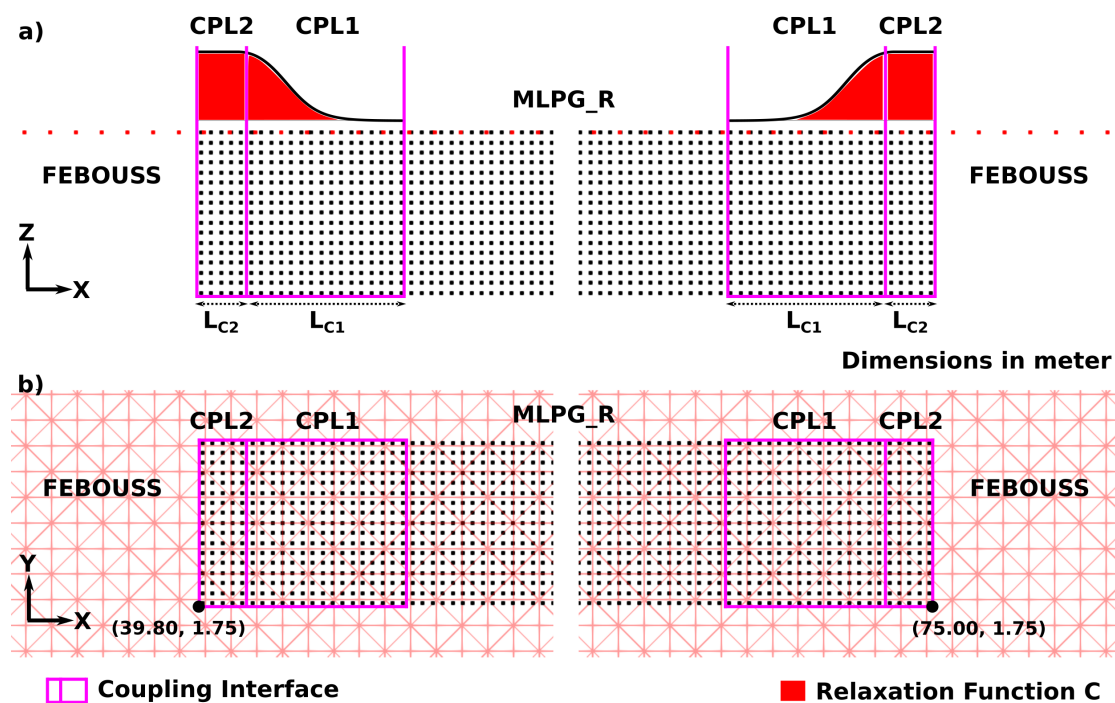


Figure 16: Schematics showing the arrangement of the FEBOUSS domain and the MLPG\_R domain near the two coupling interfaces. The schematics also show the regions defining the relaxation zone CPL1 nodes and buffer zone CPL2 nodes. Further, the part a) The side-view of the domain, additionally depicting the relaxation function  $C$  at both the coupling interfaces, with  $\alpha = 0.29, \beta = 5.0$  within the relaxation zone. b) The top-view of the domain.

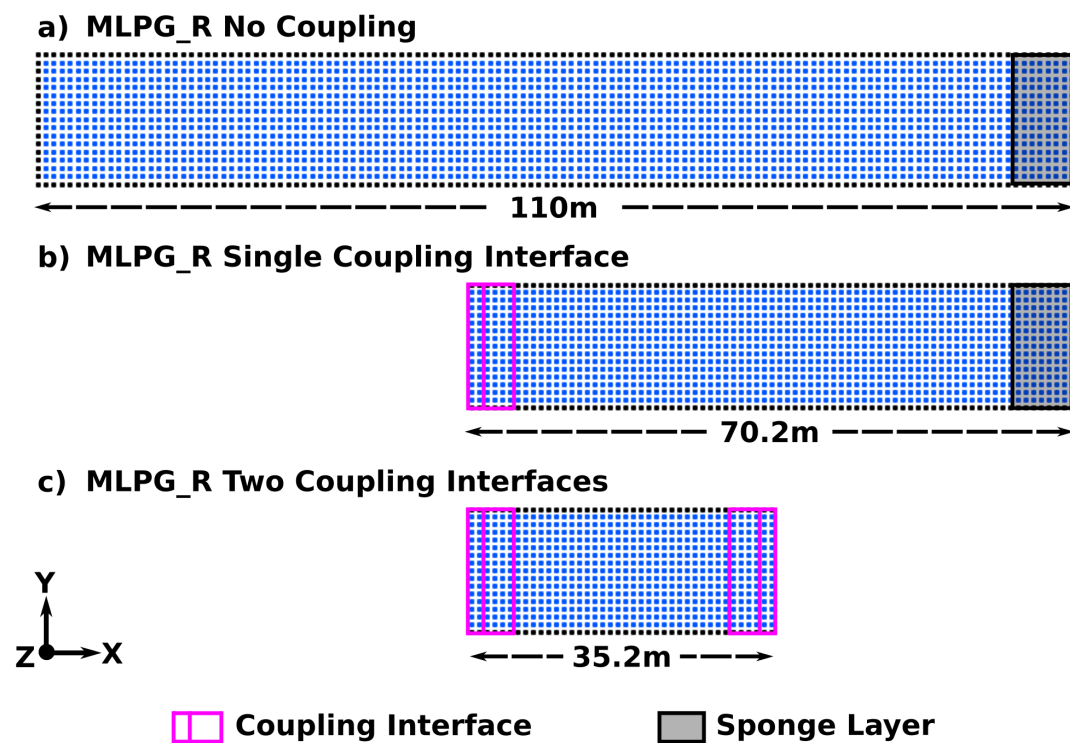


Figure 17: Top view of the MLPG\_R domains, depicting its relative size in the simulations with and without coupling interface. a) Purely MLPG\_R simulation with no coupling. b) Hybrid model with single coupling interface. c) Hybrid model with two coupling interfaces.

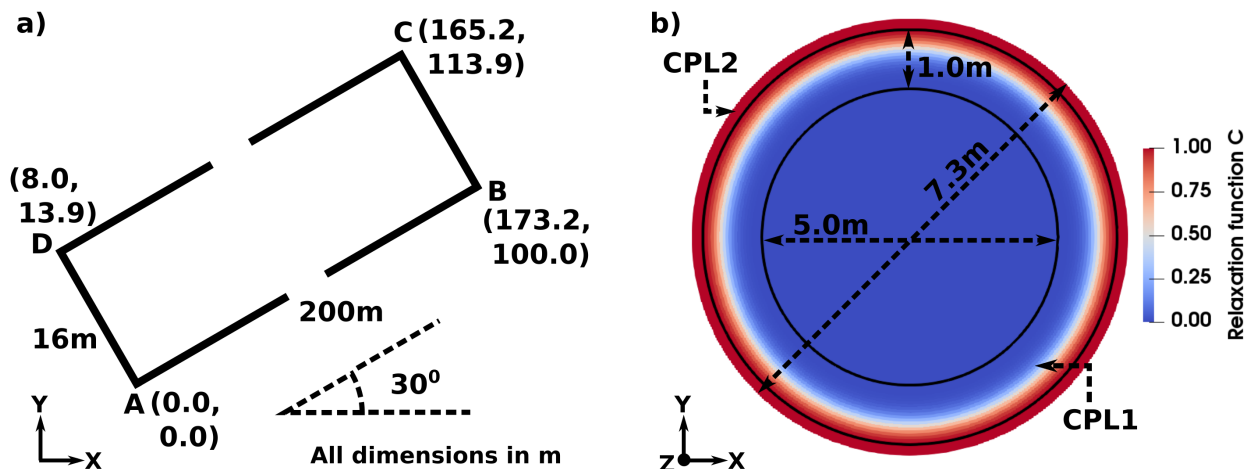


Figure 18: a) Schematic showing the rectangular FEBOUSS domain rotated anti-clockwise along the Z-axis about (0m, 0m, 0m). b) The top-view of MLPG\_R sub-domain at zeroth time-step, showing the CPL2 buffer zone, CPL1 relaxation zone along with the a contour plot of the relaxation function C.

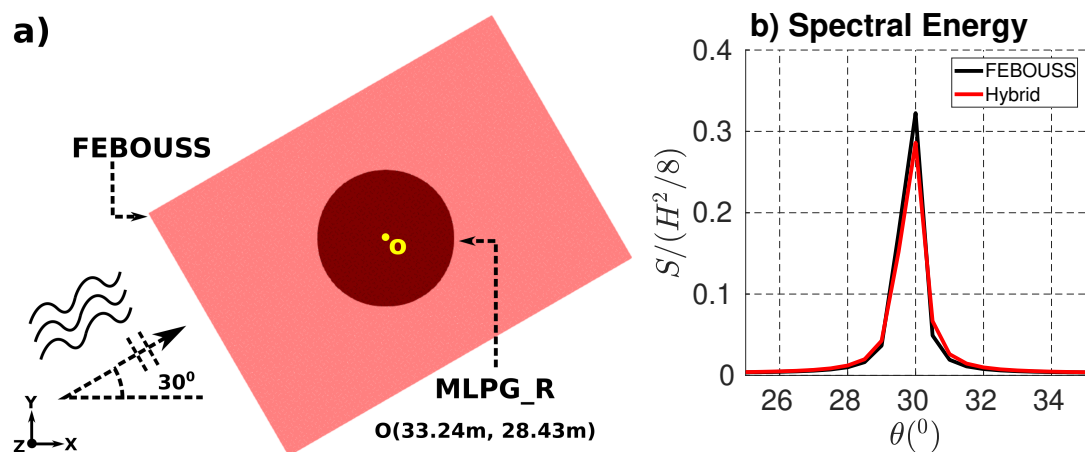


Figure 19: Schematics depicting the arrangement of FEBOUSS domain and MLPG\_R sub-domain for 3D coupling. a) Top-view showing part of FEBOUSS domain around the cylindrical MLPG\_R sub-domain, with the axis of the cylindrical MLPG\_R sub-domain at XY location  $O(33.25\text{m}, 28.43\text{m})$  at the zeroth time-step. b) Plot showing spectral energy for various directions of propagation for the wave field obtained from purely FEBOUSS and hybrid simulations around the point  $O$ .

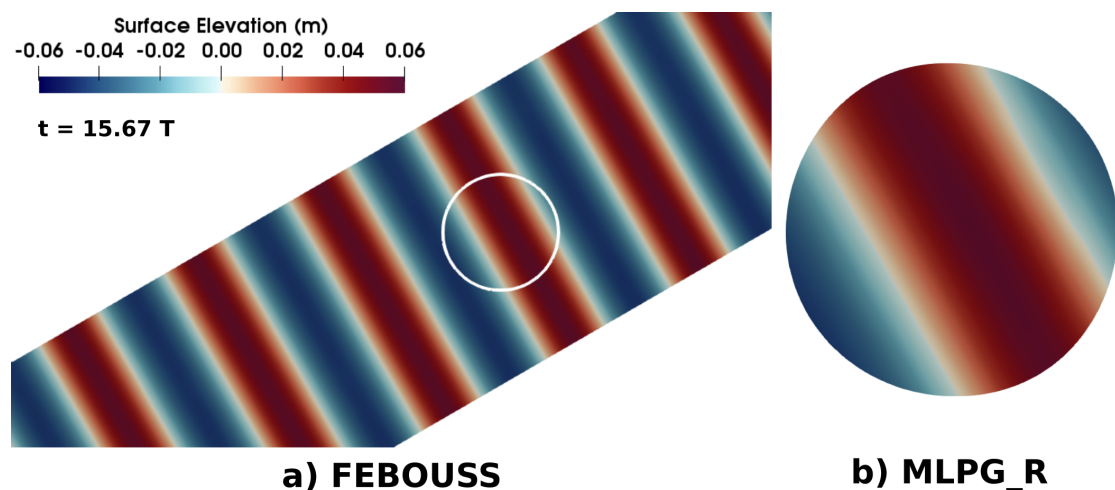


Figure 20: Results for wave-elevation contour obtained from the hybrid model at  $t = 15.67T$ . a) Contour plot from the 2D FEBOUSS domain, with the outline of the MLPG\_R sub-domain highlighted using a white circle. b) Top view of the free-surface of the 3D MLPG\_R sub-domain, with contours of surface-elevation.

Table 4: Table listing the wave elevation at wave-crest and wave-trough obtained from purely MLPG\_R, purely FEBOUSS and the hybrid model at a probe located at  $(x, y) = (50.0\text{m}, 2.0\text{m})$ . The table also presents the error w.r.t MLPG\_R for the peaks of wave elevation and depth-resolved profile of  $u$  component of velocity at wave-crest and wave-trough. Here  $H$  is the specified wave-height.

Peak	Label		L1.50R0.00	L1.50R1.50
Crest	MLPG_R	$\eta_{M,C}/H$	0.5486	0.5486
	FEBOUSS	$\eta_{F,C}/H$	0.5344	0.5344
	Hybrid	$\eta_{H,C}/H$	0.5701	0.5699
	$E_{FM,C}^\eta$	%	2.59	2.59
	$E_{HM,C}^\eta$	%	3.92	3.88
	$E_{FM,C}^u$	%	0.60	0.60
	$E_{HM,C}^u$	%	2.49	2.59
Trough	MLPG_R	$\eta_{M,T}/H$	-0.4543	-0.4543
	FEBOUSS	$\eta_{F,T}/H$	-0.4658	-0.4658
	Hybrid	$\eta_{H,T}/H$	-0.4401	-0.4403
	$E_{FM,T}^\eta$	%	2.53	2.53
	$E_{HM,T}^\eta$	%	3.13	3.08
	$E_{FM,T}^u$	%	0.99	0.99
	$E_{HM,C}^u$	%	1.32	1.34

MLPG\_R sub-domain from any direction. The cylindrical domain has an outer diameter of 7.3m and initial depth of 1.0m, with the free-surface initially at  $z = 0\text{m}$  and the bottom boundary at  $z = -1\text{m}$ . Similar to previous sections, converged results are obtained for the domain consisting of nodes placed at regular interval of 0.05m along the radius, circumference and depth. The directional wave is generated in FEBOUSS and transferred to the MLPG\_R sub-domain through a cylindrical shell coupling interface. We use three layers of buffer zone CPL2 nodes, defined using a cylindrical shell with inner diameter 7.0m and outer diameter 7.3m. The relaxation zone is defined by a cylindrical shell with inner diameter 5.0m and outer diameter 7.0m, thus having a thickness of 1m, following the conclusions from section 4.3. The relaxation function is defined using Eq. (11) with coefficients  $\alpha = 0.29$  and  $\beta = 5.0$ . Here  $x_r = 0$  corresponds to diameter 7.0m and  $x_r = 1$  corresponds to diameter 5.0m at the zeroth time-step. Fig. (18b) shows the top-view of the MLPG\_R sub-domain. It highlights the CPL1 and CPL2 nodes of the coupling interface and presents a contour plot of the relaxation function C. This cylindrical MLPG\_R sub-domain is placed within the FEBOUSS domain, with its axis at the location  $(x, y) = (33.24\text{m}, 28.43\text{m})$  at the zeroth time-step, annotated as point  $O$  in Fig. (19a). The hybrid model is executed at a constant time-step of  $\Delta t = 0.008\text{s}$ , with Courant number  $Cou = 0.15$  in the FEBOUSS domain and  $Cou = 0.50$  in the MLPG\_R sub-domain.

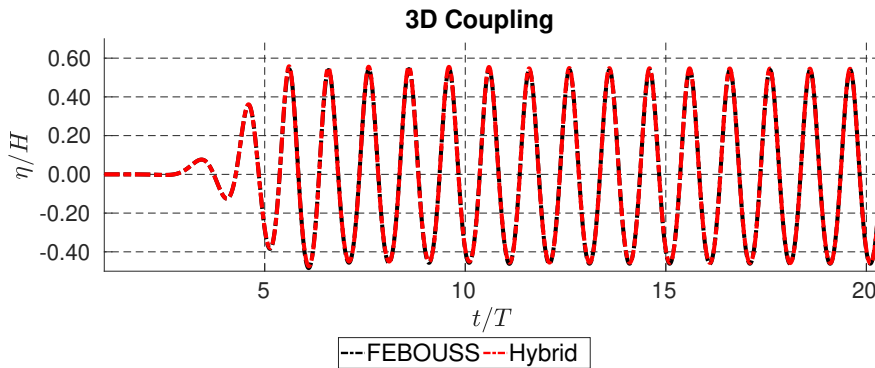
The resultant wave-elevation contours obtained from the simulation of this directional wave case in the hybrid model are presented in Fig. (20). The elevation and depth-resolved pro-

file of velocity were measured at probes located at point  $O$  in the purely FEBOUSS simulation and the MLPG\_R sub-domain of the hybrid simulation. Fig. (21) shows a comparison between the surface-elevation time-series obtained from these two simulations. This comparison contrasts the difference between the desired results from FEBOUSS against the obtained result in the MLPG\_R sub-domain from the hybrid model with FEBOUSS input. We observe an excellent agreement between the two time-series. Similar to section 4.3, we quantify the difference using relative amplitude  $A_{r,HF} = 1.0029$  (largely due to higher crests) and phase-difference  $P_{d,HF} = 0.0185$ . Please note that these error values are smaller compared to the results in section 4.3. This is because, in the presented 3D coupling setup, the coupling interface surrounds the analysis location with a relatively closer radial distance of 2.5m, compared to the previous section. Therefore, the relaxation zone smoothens the marginal phase difference between FEBOUSS and MLPG\_R sub-domains relatively sooner. Additional investigation was done for determining the dominant direction of wave propagation in purely FEBOUSS domain and MLPG\_R sub-domain of the hybrid simulation. This was achieved using wave-elevation time series from a grid of probes around the point  $O$ . The directional spectrum was calculated by maximum likelihood method using the WAFO toolbox [62]. The resultant spectral energy  $S$  for propagation angles obtained from both the simulations is shown in Fig. (19b). A dominant peak is observed in both the results at  $30^\circ$ , further validating the propagation direction.

A comparison of the depth-resolved profile for the  $u$  and  $v$  components of velocities obtained from the purely FEBOUSS,

Table 5: Table listing the wall-clock run-time for purely MLPG\_R and the hybrid simulations, thus highlighting the numerical gains from the hybrid approach.

Label			No coupling	Hybrid L1.50R0.00	Hybrid L1.50R1.50
MLPG_R domain length		(m) (%)	110.0	70.2 (63.82% of 110m)	35.2 (32.00% of 110m)
Run time	Total	(h) (%)	A 12.54	B 8.93 (71.21% of A)	C 4.42 (35.25% of A)
	MLPG_R	(h) (%)	12.54 (100% of A)	7.98 (89.44% of B)	3.50 (79.20% of C)
	FEBOUSS	(h) (%)	- -	0.91 (10.19% of B)	0.86 (19.45% of C)
	Coupling	(h) (%)	- -	0.03 (0.38% of B)	0.06 (1.35% of C)

Figure 21: Wave-elevation time series obtained at point  $O$  from purely FEBOUSS and hybrid simulations for the directional wave case with 3D coupling.

purely MLPG\_R and the hybrid simulation is shown in Fig. (22). The error in the result from hybrid model is quantified against the purely MLPG\_R result as  $E_{HMC}^u = 2.54\%$  and  $E_{HMC}^v = 1.95\%$  (see section 4.3 for definition of the errors). We observe a positive drift in both velocity components from the coupled simulation, similar to the previous conclusions. However the error for both the components is within acceptable range.

#### 4.6. Hybrid model: 3D coupling with structure

The previous sections demonstrate and provide an improved understanding of 3D coupling between the mesh based Boussinesq equation model and the particle based Navier-Stokes model. The present section builds upon these procedures for simulating interaction of regular waves with a fixed cylinder using the hybrid model. We consider a regular wave test case from a series of experiments from [63, 64] on interaction of fixed and moving cylinder with regular and focusing waves. The experimental setup consists of a cylinder of diameter 0.22m suspended from a movable trolley. The experiments measure wave-elevation at multiple probes, including some in the vicinity of the cylinder. They also report pressure at various points on the cylinder, including the stagnation point at various depths. The complete details for the setup are given in [63] with further interpretation of the results in [64].

The simulations are carried out for a regular wave with time period  $T = 2.0\text{s}$ , wave-height  $H = 0.10\text{m}$  in water depth of  $h = 0.7\text{m}$ . The coefficients corresponding to this wave are listed in Table 2 labelled as case-E2, with the Ursell number of  $Ur = 6.23$  indicating a highly asymmetric wave near the limits of Stokes-2<sup>nd</sup> order theory as shown in the wave-theory regime plot Fig. (3). Table 6 lists the position of the cylinder and probes in the experiment wave-tank, assuming the origin at the centre of the cylinder, with the X-axis along the length of the wave-tank and  $z = 0$  at still-water level. The wave propagates at  $0^\circ$  w.r.t X-axis along the length of the wave-tank. The wave-probe WP5 is placed just upwind of the cylinder to confirm the wave impacting the cylinder. The pressure probes PP2-4 are located at various depths on the stagnation point, with PP4 located above the initial water level and hence will undergo wetting and drying. Finally, pressure probes PP6 and PP8 are placed  $20^\circ$  and  $180^\circ$  from the stagnation point at a submerged depth.

In the hybrid model, instead of simulating the wave along the X-axis, we prescribe the wave-direction as  $30^\circ$  w.r.t the X-axis. Once again, similar to section 4.5, this is done to involve both  $u$  and  $v$  components of velocity in the coupling algorithm and demonstrate the 3D coupling capabilities of the interface. Given that a vertical cylinder is symmetric about its axis, we can correlate the experimental results for  $0^\circ$  wave-direction with the hybrid simulation results for  $30^\circ$  wave-direction by rotating

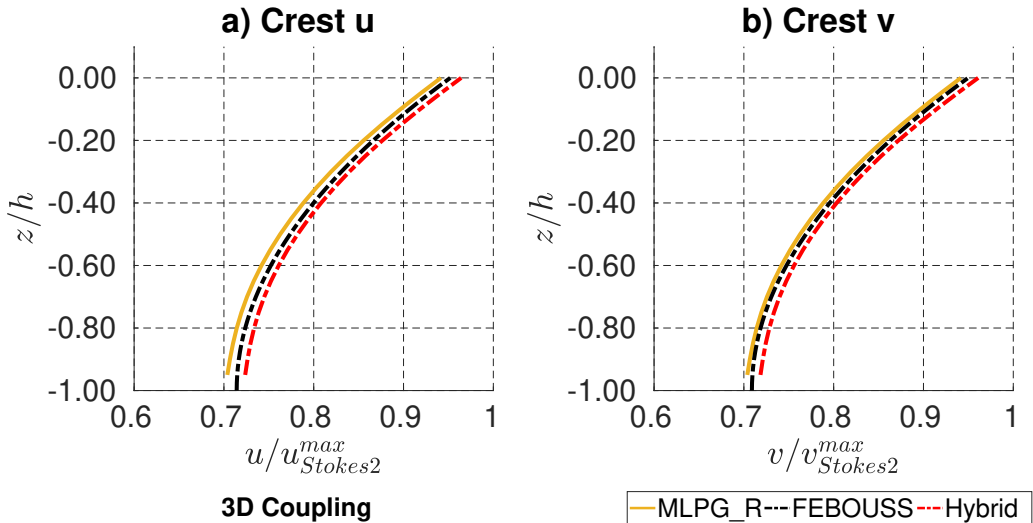


Figure 22: Plots for depth-resolved profile of the velocity components obtained from purely FEBOUSS, purely MLPG.R and hybrid simulations, under the wave-crest at point  $O$ . The velocity values are scaled against the maximum of Stokes- $2^{nd}$  order results. Here  $h$  is the still-water depth. a)  $u$  velocity component along X-axis. b)  $v$  velocity component along Y-axis.

the position of the probes in the simulation setup by  $30^\circ$  anti-clockwise. Table 6 thus lists the positions of the same probes in the MLPG.R sub-domain of the hybrid simulation, obtained by rotating the experimental locations anti-clockwise by  $30^\circ$  about the Z-axis at the origin.

The MLPG.R sub-domain is a cylinder with its axis along the Z-axis, centred at  $(x, y) = (0\text{m}, 0\text{m})$ . It has an outer-diameter 5.4m and initial depth of 0.7m, with the free-surface initially at  $z = 0\text{m}$  and bottom boundary at  $z = -0.7\text{m}$ . The MLPG.R sub-domain consists of a vertical cylindrical structure of diameter 0.22m centred at  $(x, y) = (0\text{m}, 0\text{m})$ , having a height 1.0m between  $z = -0.7\text{m}$  and  $z = 0.3\text{m}$ . The fluid domain is bound by the free-surface on the top, and slip walls at the bottom and at the vertical cylindrical structure. The waves are generated and absorbed in the MLPG.R sub-domain using a cylindrical shell coupling interface with FEBOUSS input, similar to Fig. (18b). Here the buffer zone nodes are places between diameter 5.40m and 4.98m, and a 0.7m wide relaxation zone between diameter 4.98m and 3.58m. The relaxation function is defined by Eq. (11) with  $\alpha = 0.29, \beta = 5.0$ , where  $x_r = 0$  corresponds to diameter 4.98m and  $x_r = 1$  corresponds to diameter 3.58m. Converged results were obtained using particles distributed at a regular interval of  $0.035\text{m} = h/20$ . Fig. (23a) shows the top view of the MLPG.R sub-domain containing the cylindrical structure in the centre, with depiction of buffer zone and relaxation zone along with contour plot of relaxation function at the zeroth time-step. It also highlights the position of the MLPG.R sub-domain surrounded by the rectangular FEBOUSS domain for wave generation. Further, Fig. (23a) and Fig. (23b) show the position of the aforementioned wave probe relative to the cylinder and the pressure-probes on the cylinder within the MLPG.R sub-domain.

The FEBOUSS domain is rectangular tank of length 90m  $\approx 19.5L$  and width 10m in the XY plane which is rotated anti-clockwise about the Z-axis by  $30^\circ$  for consistently generating

directional waves. It encompasses the MLPG.R sub-domain, with the 4 corners of the rectangular domain located as shown in Fig. (23a). The domain has a constant depth of  $h = 0.7\text{m}$  and is bounded by a wave-maker at boundary DA, slip walls at boundaries AB and CD and a  $2.5L$  long sponge layer adjacent to the boundary BC. Using the conclusions from section 4.1, it is meshed using regularly spaced points at an interval of  $0.08\text{m} = L/57.80$ , connected by right angled triangles. The hybrid model is executed at a constant time-step of  $\Delta t = 0.00625\text{s}$ , resulting in Courant number  $Cou = 0.21$  in the FEBOUSS domain and  $Cou = 0.47$  in the MLPG.R sub-domain.

This setup for the hybrid simulation generates successive directional regular waves in the MLPG.R sub-domain using the velocity input from the FEBOUSS simulation. Fig. (24a) presents a contour plot of the surface elevation in the top-view of the MLPG.R sub-domain, showcasing the interaction of a wave-crest with the vertical cylinder at  $t = 10.5T$ . Fig. (24b) presents a contour plot of the magnitude of the 3D velocity vector at the free-surface using a top-view of the MLPG.R domain at the same time-instance. The corresponding velocity vector plot at the free-surface in the XY plane is shown in Fig. (25a), while Fig. (25b) shows the same for particles in a slice along the mid-line of the cylinder in the XZ plane. These figures show a snapshot of the 3D flow around the cylinder, with the wave-crest located immediately behind the cylinder. As the wave-crest approaches the cylinder, the flow would run-up vertically along the stagnation point on the cylinder, at positions corresponding to pressure probes PP2-4. The presented time-instance is the run-down of this flow with the receding wave-crest as seen in Fig. (25b). At this stage, the horizontal components of particle velocities will still be predominantly aligned along the wave-direction. However, with the presence of the cylinder, the flow has to navigate around the structure, accelerating to maximum velocity and finally converging back behind the cylinder, as shown in Fig. (25a). However, due to inertia, a local low veloc-

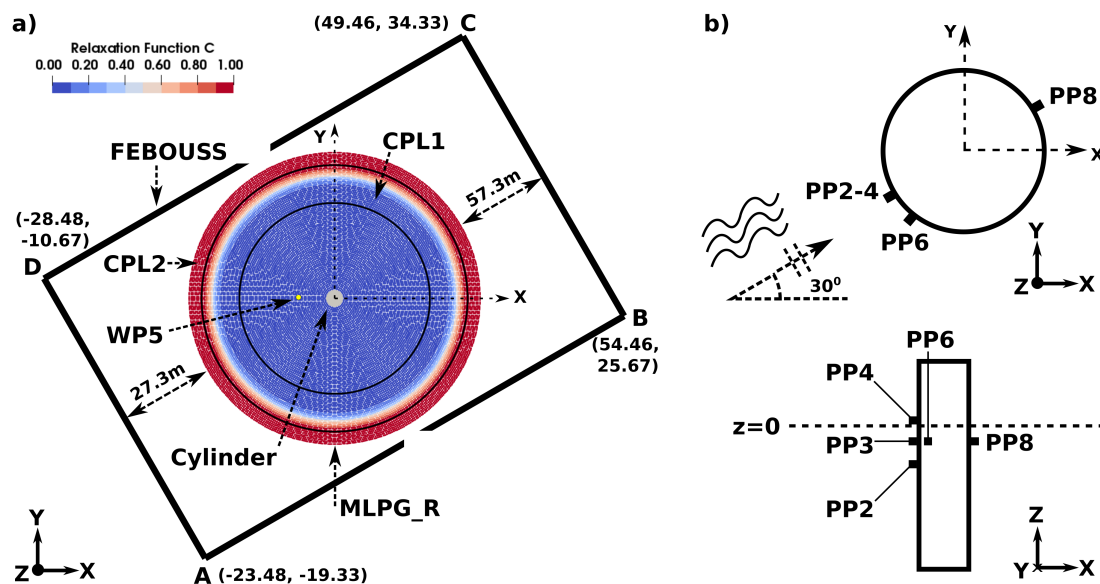


Figure 23: a) Schematic of the MLPG\_R sub-domain located within the rectangular FEBOUSS domain. The MLPG\_R domain is shown with the vertical cylindrical structure at its centre, the buffer zone CPL2 and relaxation zone CPL1 of the coupling interface for wave generation and absorption and location of WP5. b) Schematics for position of the pressure probes on the vertical cylindrical structure within the MLPG\_R sub-domain.

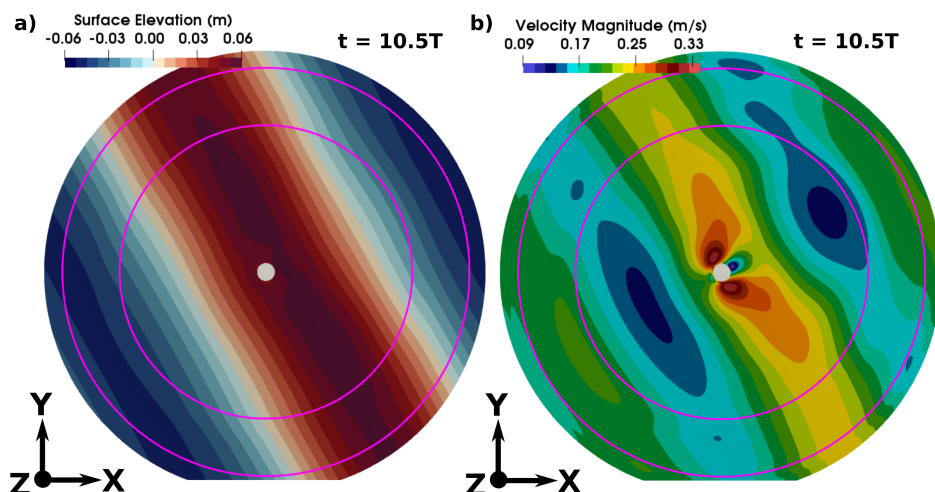


Figure 24: Top-view of the free-surface of MLPG\_R sub-domain showing contour plots for interaction of a wave-crest with the vertical cylindrical structure. a) Contour plot of surface-elevation  $\eta$ . b) Contour plot of magnitude of 3D velocity vector at the moving free-surface. The pink lines indicate the region of the relaxation zone.

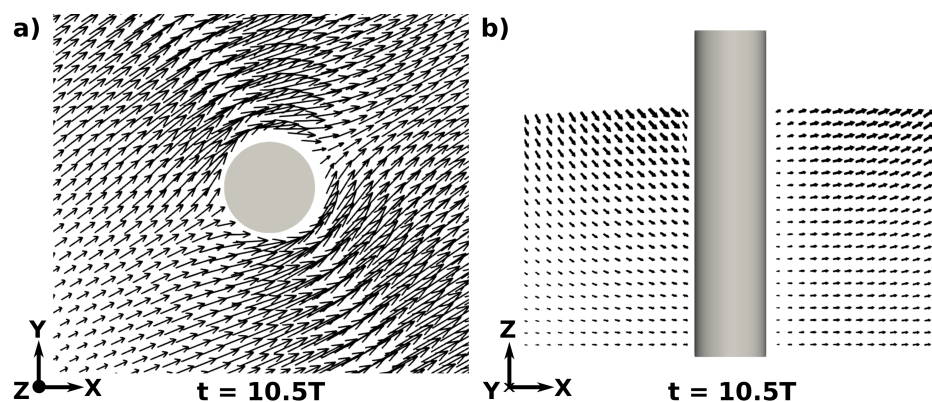


Figure 25: Quiver plot show the flow velocity vector in the vicinity of the cylinder. a) Top view of the moving free-surface. b) Side view of a slice of particles along the mid-line of the cylinder.

Table 6: Table listing the positions of the cylinder, wave-probe and pressure probe in the experimental setup for wave-direction  $0^\circ$  and the hybrid simulation setup for the wave-direction  $30^\circ$ .

Label	Experiment Wave Direction $0^\circ$			Simulation Wave Direction $30^\circ$			Relative error	
	X (m)	Y (m)	Z (m)	X (m)	Y (m)	Z (m)	$A_{r,HE}$	$A_{r,HM}$
Cylinder Centre	0.0	0.0	-	0.0	0.0	-		
WP5	-0.570	0.260	-	-0.624	-0.060	-		
PP2	-0.110	0.0	-0.185	-0.096	-0.056	-0.185	1.069	1.020
PP3	-0.110	0.0	-0.085	-0.096	-0.056	-0.085	1.071	1.021
PP4	-0.110	0.0	0.015	-0.096	-0.056	0.015	1.041	1.008
PP6	-0.104	-0.038	-0.085	-0.071	-0.085	-0.085	1.066	1.022
PP8	0.110	0.0	-0.085	-0.096	-0.056	-0.085	0.923	1.039

ity region is observed behind the cylinder, as seen in the velocity contour plot Fig. (24b), despite the presence of the wave-crest at that location.

The surface elevation at WP5 and pressure time-series at PP2-8 obtained from the hybrid simulation are compared against experimental results reported in [63, 64] and numerical results from purely MLPG\_R simulation reported in [2]. The comparison is further quantified between time interval  $t \in [11, 13]T$  using the relative amplitude parameter  $A_r$ . Here  $A_{r,HM}$  is the error in pressure  $p_H$  from hybrid model with respect to purely MLPG result  $p_M$ , while  $A_{r,HE}$  is the comparison against the experimental pressure  $p_E$ .

$$A_{r,HM} = \sqrt{\frac{\sum_t (p_H)^2}{\sum_t (p_M)^2}}, \quad A_{r,HE} = \sqrt{\frac{\sum_t (p_H)^2}{\sum_t (p_E)^2}} \quad (14)$$

A value of  $A_r \rightarrow 1$  indicates a perfect agreement between the two time-series, while a  $A_r > 1$  and  $A_r < 1$  indicate over-prediction and under-prediction of magnitudes, respectively. Fig. (26) shows the comparison between the three results for every probe. The surface elevation results at WP5 shows an excellent match between the three time-series. The wave-height from the hybrid model is 1.26% higher than the experiment and 0.94% higher than purely MLPG\_R result. The pressure from the hybrid model is marginally higher than purely MLPG\_R results for probes PP2, PP3, PP4 and PP6, each having  $A_{r,HM} \approx 1.020$ . The majority of this error is due to the difference in their profiles between the trough and the zero up-crossing. The only major difference between the two numerical results is at PP8 at the rear stagnation point, where the magnitude of trough pressure is higher in the hybrid result by 7.93% compared to the purely MLPG\_R result. We can further observe a reasonable comparison of pressure time-series against the experiment, with the hybrid simulation producing higher peaks

for the upwind probes PP2-4 and troughs with lower magnitude for the downwind probe PP8. However, the same trend is also observed when comparing the purely MLPG\_R results against the experiments, which indicates that these errors are not originating from the coupling interface. This example thus demonstrates the ability of the hybrid model to produce results reasonably similar to purely MLPG\_R simulation for the presented case of wave-structure interaction. Fig. (27) presents a 3D rendition of the simulated case, showcasing the final arrangement and result of hybrid model, with the FEBOUSS domain surrounding the local MLPG\_R sub-domain.

## 5. Conclusion

The manuscript presented procedures and their application for one-way coupling of mesh-based Boussinesq equation model with particle-based Navier-Stokes model in 3D. The finite-element model for depth-integrated form of Boussinesq equations can model 3D wave-transformation using a 2D surface mesh, thus allowing analysis over large domains. It is referred to as FEBOUSS in the manuscript. The Navier-Stokes equations for incompressible flow were modelled using the MLPG\_R method following the projection scheme. The key differentiating feature for this method is the solution of the pressure Poisson equation in weak-form using Rankine source test function, which crucially eliminates derivatives of unknown variables.

The paper discusses two crucial aspects of one-way coupling between these two numerical models, 1) calculation of depth-resolved quantities in FEBOUSS, 2) formulation of coupling interface in the MLPG\_R domain. The algorithm for calculation of depth-resolved quantities from the depth-integrated velocities of FEBOUSS was presented, where the spatial deriva-

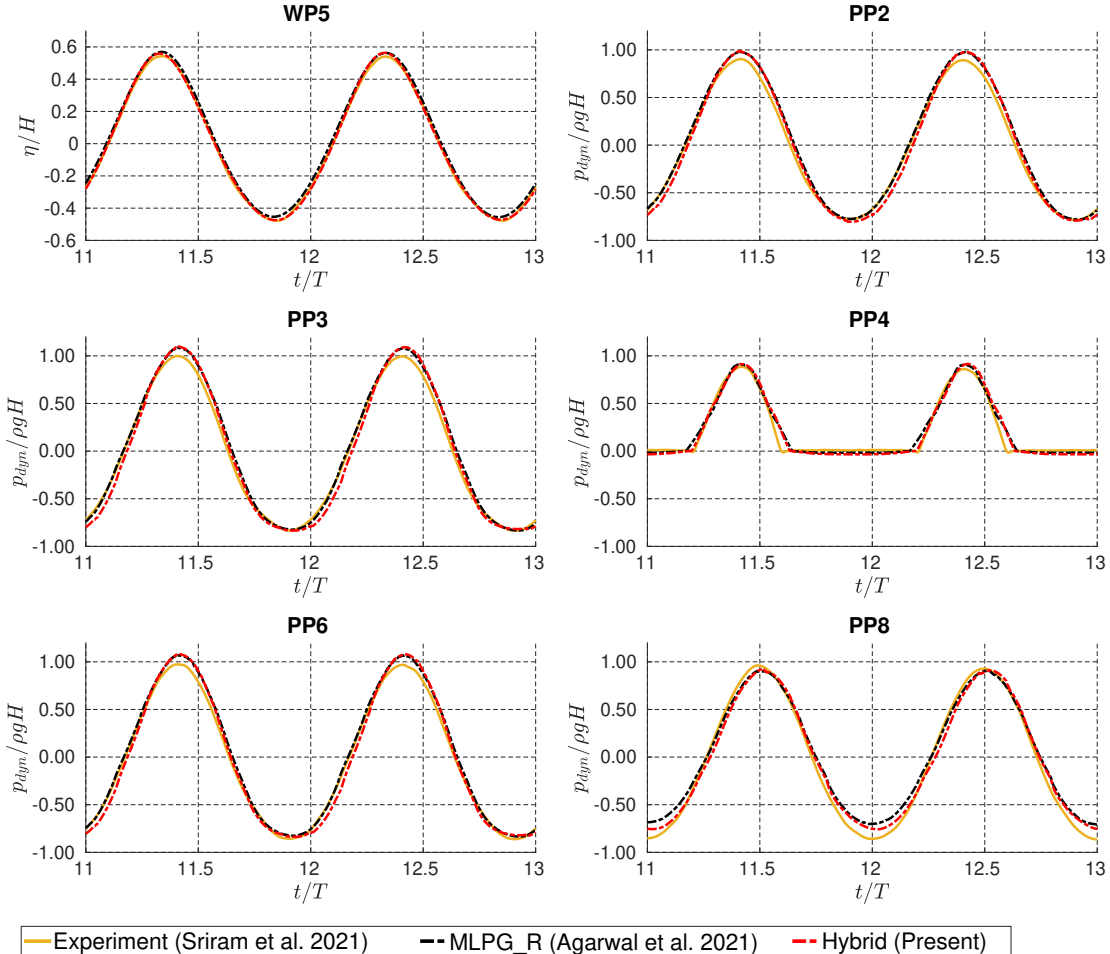


Figure 26: Plots for time-series of surface elevation at WP5 and pressure at PP2-8, obtained from experimental results of [63], numerical results from purely MLPG\_R model of [2] and numerical results from the presented hybrid model.

tives at the mesh nodes were evaluated using a mesh-less approach. The algorithm was tested for various regular waves, ranging from shallow to intermediate depths within the Stokes- $2^{nd}$  order theory regime and its comparison against theory and other numerical models was presented. An excellent agreement for the surface-elevation from FEBOUSS is reported for all tested cases. Among the depth resolved quantities, an agreeable comparison for the velocities is observed, with increasing error in the depth-resolved profile for deeper waves. This is primarily due to the error in the perturbation method based expression for the velocities. However, the results obtained for depth-resolved pressure from FEBOUSS were relatively poor, primarily due to the requirement of time-derivative. A further validation was carried against experimental measurements for wave-transformation over a submerged bar. The paper reports a fair comparison for the horizontal component of velocity under the wave crest and trough against the experimental results. In contrast with a finite-difference model, FEBOUSS did not require additional smoothing of the spatial derivatives, resulting in better comparison of the depth-resolved velocities.

The coupling interface in MLPG\_R domain was implemented using a moving relaxation zone and a detailed discus-

sion on its implementation was presented. Test cases with single coupling interface for wave generation and two coupling interfaces for wave generation and absorption were presented, with further investigation of the size of the relaxation zone. The results from hybrid model produces the desired wave-height with error within 1%, but has a higher peak of at-most 3.9% when compared with purely MLPG\_R solution. Similarly, the velocity profile under a wave-crest from the hybrid result is over-estimated by 2.6% for the tested cases. The length of the relaxation zone is reported to have minimal influence on the result. However, it is found to impact the distribution of the Lagrangian particle within the relaxation zone due to the divergent flow within this region. The hybrid model for these tests is reported to take 35.3% of the computation time compared to purely MLPG\_R simulation.

The coupling capability for 3D cases is demonstrated using a direction wave case. The MLPG\_R sub-domain within the hybrid model initially has a cylindrical shape, with a cylindrical shell coupling interface surrounding the region of interest. The results from the hybrid model are once again reported to have a fair comparison against purely MLPG\_R solution, with 2–3% over-prediction of peak elevation and horizontal compo-

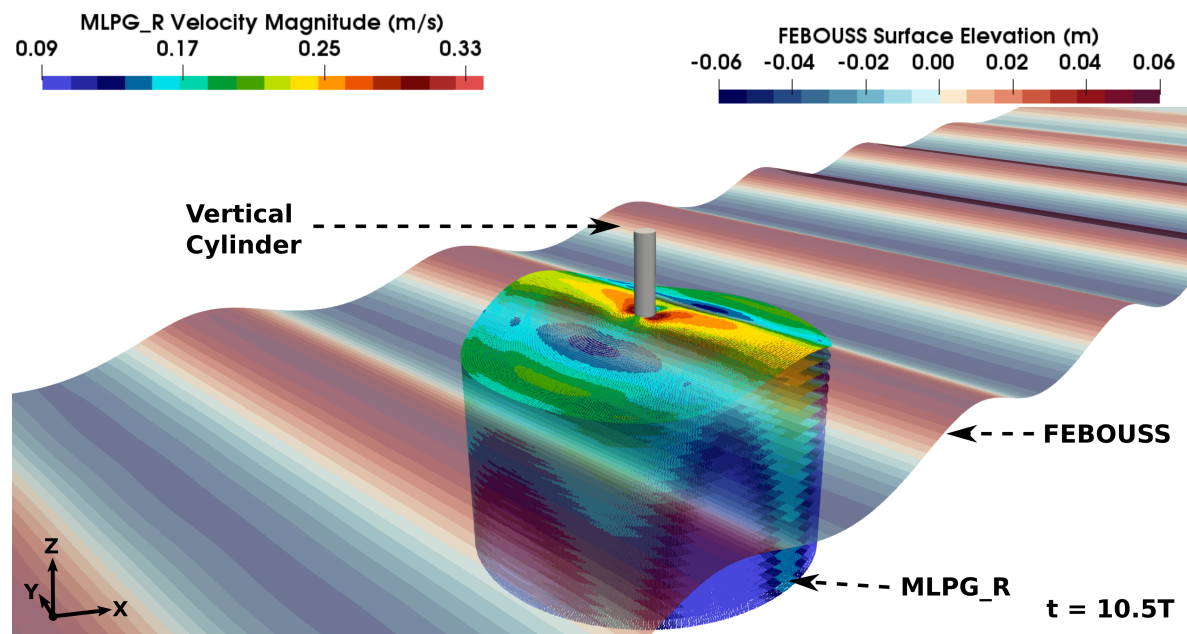


Figure 27: A 3D rendition of the hybrid model, showing the transparent FEBOUSS domain with contours of surface elevation surrounding the 3D MLPG\_R domain with contours of magnitude of velocity.

nents of velocity along X and Y axes. Finally, the interaction of a vertical cylinder with a directional regular wave is simulated using the hybrid model in 3D. The results for wave and pressure probes are reported to have excellent agreement with purely MLPG\_R simulation, with marginal over-prediction of peaks for upwind probes and 7.93% over-prediction of trough magnitude at the downwind probe. Due to the weakly-dispersive FEBOUSS, the presented hybrid model will be limited to coastal and near-shore applications. However, the coupling algorithm and analysis presented in this manuscript form the basis for coupling particle-based Navier-Stokes models with improved Boussinesq-type models for deep-water applications.

The presented hybrid model thus can enable analysis of large domain problems, with local particle-based sub-domains in regions around structures. It should be noted that hybrid models are not developed only for improving computational efficiency. They also allow exposing structures to realistic waves that have transformed over various idiosyncrasies of a coastal region. This manuscript presented regular-wave test cases to study the accuracy and robustness of the coupled solution. However, the true capabilities of this hybrid model will be demonstrated in our future work through multi-directional and irregular waves. Additional research will be conducted to study the influence of the internal MLPG\_R domain size on the hybrid solution in presence of complex structures and for various wave characteristics. This hybrid model also reduces the number of nodes in the MLPG\_R domain. This can potentially allow use of coarser distribution within MLPG\_R domain due to reduction in accumulated error. These aspects of the hybrid model will require further investigation. The presented 3D hybrid model sets up the basis for such future research.

## 6. Acknowledgement

The first author acknowledges the support of Prime Minister's Research Fellowship (PMRF), India in funding this research work. We acknowledge the use of the computing resources at HPCE, Indian Institute of Technology Madras. The second author would like to thank DST-INSPIRE.

## Author ORCIDs

**S. Agarwal:** <https://orcid.org/0000-0003-1922-4242>

**V. Sriram:** <https://orcid.org/0000-0003-3586-9577>

**K. Murali:** <https://orcid.org/0000-0002-4251-841X>

## Author contributions

**S. Agarwal:** Conceptualisation, Software, Validation, Formal analysis, Methodology, Writing - Original Draft, Visualisation.

**V. Sriram:** Conceptualisation, Methodology, Writing – review and editing, Funding acquisition, Supervision. **K. Murali:** Writing – review and editing, Funding acquisition, Supervision.

## References

- [1] S. Agarwal, V. Sriram, P.-F. Liu, K. Murali, Waves in waterways generated by moving pressure field in Boussinesq equations using unstructured finite element model, *Ocean Engineering* 262 (2022) 112202. [doi:10.1016/j.oceaneng.2022.112202](https://doi.org/10.1016/j.oceaneng.2022.112202).
- [2] S. Agarwal, V. Sriram, S. Yan, K. Murali, Improvements in MLPG formulation for 3D wave interaction with fixed structures, *Computers & Fluids* 218 (2021) 104826. [doi:<https://doi.org/10.1016/j.compfluid.2020.104826>](https://doi.org/10.1016/j.compfluid.2020.104826).

- [3] V. Sriram, S. Agarwal, S. Yan, Z. Xie, S. Saincher, et al., A comparative study on the nonlinear interaction between a focusing wave and cylinder using state-of-the-art solvers: Part A, International Journal of Offshore and Polar Engineering 31 (1) (2021) 1–10. [doi:10.17736/ijope.2021.jc820](https://doi.org/10.17736/ijope.2021.jc820).
- [4] P. Ferrant, L. Gentaz, B. Alessandrini, R. Luquet, C. Monroy, G. Ducrozet, E. Jacquin, A. Drouet, Fully nonlinear potential/RANSE simulation of wave interaction with ships and marine structures, Proceedings of the International Conference on Offshore Mechanics and Arctic Engineering - OMAE 6 (2008) 379 – 387. [doi:10.1115/OMAE2008-57952](https://doi.org/10.1115/OMAE2008-57952).
- [5] Y. Zhang, G. Reliquet, B. Bouscasse, L. Gentaz, D. Le Touzé, Numerical Investigation on the Added Resistance and Seakeeping Performance of KVLCC2 with the SWENSE Method, Journal of Ship Research 65 (04) (2021) 362–379. [doi:10.5957/JOSR.03200023](https://doi.org/10.5957/JOSR.03200023).
- [6] Q. W. Ma, S. Yan, QALE-FEM for numerical modelling of non-linear interaction between 3D moored floating bodies and steep waves, International Journal for Numerical Methods in Engineering 78 (6) (2009) 713–756. [doi:https://doi.org/10.1002/nme.2505](https://doi.org/10.1002/nme.2505).
- [7] V. Sriram, T. Schlurmann, S. Schimmels, Focused wave evolution using linear and second order wavemaker theory, Applied Ocean Research 53 (2015) 279–296. [doi:10.1016/j.apor.2015.09.007](https://doi.org/10.1016/j.apor.2015.09.007).
- [8] A. Engsig-Karup, H. Bingham, O. Lindberg, An efficient flexible-order model for 3d nonlinear water waves, Journal of Computational Physics 228 (6) (2009) 2100–2118. [doi:https://doi.org/10.1016/j.jcp.2008.11.028](https://doi.org/10.1016/j.jcp.2008.11.028).
- [9] F. Shi, J. T. Kirby, J. C. Harris, J. D. Geiman, S. T. Grilli, A high-order adaptive time-stepping TVD solver for Boussinesq modeling of breaking waves and coastal inundation, Ocean Modelling 43–44 (2012) 36–51. [doi:https://doi.org/10.1016/j.ocemod.2011.12.004](https://doi.org/10.1016/j.ocemod.2011.12.004).
- [10] P. J. Lynett, T.-R. Wu, P. L.-F. Liu, Modeling wave runup with depth-integrated equations, Coastal Engineering 46 (2) (2002) 89–107. [doi:10.1016/S0378-3839\(02\)00043-1](https://doi.org/10.1016/S0378-3839(02)00043-1).
- [11] M. Zijlema, G. Stelling, P. Smit, SWASH: An operational public domain code for simulating wave fields and rapidly varied flows in coastal waters, Coastal Engineering 58 (10) (2011) 992–1012. [doi:https://doi.org/10.1016/j.coastaleng.2011.05.015](https://doi.org/10.1016/j.coastaleng.2011.05.015).
- [12] G. Ducrozet, F. Bonnefoy, D. Le Touzé, P. Ferrant, HOS-ocean: Open-source solver for nonlinear waves in open ocean based on High-Order Spectral method, Computer Physics Communications 203 (2016) 245–254. [doi:https://doi.org/10.1016/j.cpc.2016.02.017](https://doi.org/10.1016/j.cpc.2016.02.017).
- [13] J. Wang, Q. Ma, S. Yan, A fully nonlinear numerical method for modeling wave-current interactions, Journal of Computational Physics 369 (2018) 173–190. [doi:10.1016/j.jcp.2018.04.057](https://doi.org/10.1016/j.jcp.2018.04.057).
- [14] L. Chen, J. Zang, A. Hillis, G. Morgan, A. Plummer, Numerical investigation of wave-structure interaction using OpenFOAM, Ocean Engineering 88 (2014) 91–109. [doi:https://doi.org/10.1016/j.oceaneng.2014.06.003](https://doi.org/10.1016/j.oceaneng.2014.06.003).
- [15] Z. Xie, T. Stoesser, S. Yan, Q. Ma, P. Lin, A cartesian cut-cell based multiphase flow model for large-eddy simulation of three-dimensional wave-structure interaction, Computers & Fluids 213 (2020) 104747. [doi:https://doi.org/10.1016/j.compfluid.2020.104747](https://doi.org/10.1016/j.compfluid.2020.104747).
- [16] A. Christou, T. Stoesser, Z. Xie, A large-eddy-simulation-based numerical wave tank for three-dimensional wave-structure interaction, Computers & Fluids 231 (2021) 105179. [doi:https://doi.org/10.1016/j.compfluid.2021.105179](https://doi.org/10.1016/j.compfluid.2021.105179).
- [17] J. Monaghan, Simulating free surface flows with SPH, Journal of Computational Physics 110 (2) (1994) 399–406. [arXiv:arXiv:1011.1669v3](https://arxiv.org/abs/arXiv:1011.1669v3), [doi:10.1006/jcph.1994.1034](https://doi.org/10.1006/jcph.1994.1034).
- [18] A. Crespo, J. Domínguez, B. Rogers, M. Gómez-Gesteira, S. Longshaw, R. Canelas, R. Vacondio, A. Barreiro, O. García-Feal, DualSPHysics: Open-source parallel CFD solver based on Smoothed Particle Hydrodynamics (SPH), Computer Physics Communications 187 (2015) 204–216. [doi:https://doi.org/10.1016/j.cpc.2014.10.004](https://doi.org/10.1016/j.cpc.2014.10.004).
- [19] Q. W. Ma, A new meshless interpolation scheme for MLPG\_R method, CMES - Computer Modeling in Engineering and Sciences 23 (2) (2008) 75–89.
- [20] A. Khayyer, H. Gotoh, Enhancement of stability and accuracy of the moving particle semi-implicit method, Journal of Computational Physics 230 (8) (2011) 3093–3118. [doi:https://doi.org/10.1016/j.jcp.2011.01.009](https://doi.org/10.1016/j.jcp.2011.01.009).
- [21] S. Geller, M. Krafczyk, J. Tölke, S. Turek, J. Hron, Benchmark computations based on Lattice-Boltzmann, finite element and finite volume methods for laminar flows, Computers & Fluids 35 (8) (2006) 888–897. [doi:10.1016/j.compfluid.2005.08.009](https://doi.org/10.1016/j.compfluid.2005.08.009).
- [22] C. Janßen, M. Krafczyk, Free surface flow simulations on gpgpus using the Ibm, Computers & Mathematics with Applications 61 (12) (2011) 3549–3563. [doi:https://doi.org/10.1016/j.camwa.2011.03.016](https://doi.org/10.1016/j.camwa.2011.03.016).
- [23] C. F. Janssen, S. T. Grilli, M. Krafczyk, Modeling of wave breaking and wave-structure interactions by coupling of Fully Nonlinear Potential Flow and Lattice-Boltzmann models, Proceedings of the 20th International Offshore and Polar Engineering Conference (ISOPE) 3 (2010) 686–693.
- [24] V. Sriram, Q. W. Ma, T. Schlurmann, A hybrid method for modelling two dimensional non-breaking and breaking waves, Journal of Computational Physics 272 (2014) 429–454. [doi:10.1016/j.jcp.2014.04.030](https://doi.org/10.1016/j.jcp.2014.04.030).
- [25] X. Ni, W. Feng, S. Huang, X. Zhao, X. Li, Hybrid SW-NS SPH models using open boundary conditions for simulation of free-surface flows, Ocean Engineering 196 (November 2019) (2020) 106845. [doi:10.1016/j.oceaneng.2019.106845](https://doi.org/10.1016/j.oceaneng.2019.106845).
- [26] S. Yan, Q. W. Ma, J. Wang, J. Zhou, Self-Adaptive Wave Absorbing Technique for Nonlinear Shallow Water Waves, in: Volume 1: Offshore Technology; Offshore Geotechnics, Vol. 1, American Society of Mechanical Engineers, 2016, pp. 1–8. [doi:10.1115/OMAE2016-54475](https://doi.org/10.1115/OMAE2016-54475).
- [27] K. I. Sitanggang, P. J. Lynett, Multi-scale simulation with a hybrid Boussinesq-RANS hydrodynamic model, International Journal for Numerical Methods in Fluids 62 (2009) 1013–1046. [doi:10.1002/fld.2056](https://doi.org/10.1002/fld.2056).
- [28] K. I. Sitanggang, P. J. Lynett, P. L.-F. Liu, Development of a Boussinesq-RANS VOF hybrid wave model, in: J. M. Smith (Ed.), 30th International Conference on Coastal Engineering, ICCE 2006, San Diego, CA, USA, 2007, pp. 24–35.
- [29] T. Verbrugghe, J. M. Domínguez, A. J. Crespo, C. Altomare, V. Stratigaki, P. Troch, A. Kortenhaus, Coupling methodology for smoothed particle hydrodynamics modelling of non-linear wave-structure interactions, Coastal Engineering 138 (April) (2018) 184–198. [doi:10.1016/j.coastaleng.2018.04.021](https://doi.org/10.1016/j.coastaleng.2018.04.021).
- [30] M. Narayanaswamy, A. J. C. Crespo, M. Gómez-Gesteira, R. A. Dalrymple, SPHysics-FUNWAVE hybrid model for coastal wave propagation, Journal of Hydraulic Research 48 (2010) 85–93. [doi:10.1080/00221686.2010.9641249](https://doi.org/10.1080/00221686.2010.9641249).
- [31] J. Wang, S. Yan, Q. Ma, J. Wang, Z. Xie, S. Marran, Modelling of focused wave interaction with wave energy converter models using qaleFOAM, Proceedings of the Institution of Civil Engineers: Engineering and Computational Mechanics 173 (3) (2020) 100–118. [doi:10.1680/jencm.19.00035](https://doi.org/10.1680/jencm.19.00035).
- [32] C. Altomare, B. Tagliafierro, J. Domínguez, T. Suzuki, G. Viccione, Improved relaxation zone method in SPH-based model for coastal engineering applications, Applied Ocean Research 81 (October) (2018) 15–33. [doi:10.1016/j.apor.2018.09.013](https://doi.org/10.1016/j.apor.2018.09.013).
- [33] S. Agarwal, V. Sriram, K. Murali, Interaction of Fixed Cylinder With Waves Through Weakly Coupled FNPT and Lagrangian Navier-Stokes, in: Proceedings of the ASME 2019 38th International Conference on Ocean, Offshore and Arctic Engineering. Volume 7A: Ocean Engineering, American Society of Mechanical Engineers, Glasgow, Scotland, UK, 2019, pp. 1–8. [doi:10.1115/OMAE2019-96745](https://doi.org/10.1115/OMAE2019-96745).
- [34] Q. W. Ma, MLPG method based on Rankine source solution for simulating nonlinear water waves, CMES - Computer Modeling in Engineering and Sciences 9 (2) (2005) 193–209. [doi:10.3970/cmes.2005.009.193](https://doi.org/10.3970/cmes.2005.009.193).
- [35] P. A. Madsen, O. R. Sørensen, A new form of the Boussinesq equations with improved linear dispersion characteristics. Part 2. A slowly-varying bathymetry, Coastal Engineering 18 (3-4) (1992) 183–204. [doi:10.1016/0378-3839\(92\)90019-Q](https://doi.org/10.1016/0378-3839(92)90019-Q).
- [36] O. R. Sørensen, H. A. Schäffer, L. S. Sørensen, Boussinesq-type modelling using an unstructured finite element technique, Coastal Engineering 50 (4) (2004) 181–198. [doi:10.1016/j.coastaleng.2003.10.005](https://doi.org/10.1016/j.coastaleng.2003.10.005).
- [37] Wolfram Research, Inc., Mathematica, Version 12.2, Champaign, IL (2020). URL <https://www.wolfram.com/mathematica>
- [38] P. Madsen, O. Sørensen, Bound waves and triad interactions in shallow water, Ocean Engineering 20 (4) (1993) 359–388. [doi:10.1016/0029-1990\(93\)90019-Q](https://doi.org/10.1016/0029-1990(93)90019-Q).

- 0029-8018(93)90002-Y.
- [39] R. W. Whalin, Wave refraction theory in a convergence zone, *Coastal Engineering* (1971) 451–470. [doi:10.9753/icce.v12.139](https://doi.org/10.9753/icce.v12.139).
- [40] J. C. W. Berkhoff, N. Booij, A. C. Radner, Verification of numerical wave propagation models for simple harmonic linear water waves, *Coastal Engineering* 6 (3) (1982) 255–279. [doi:10.1016/0378-3839\(82\)90022-9](https://doi.org/10.1016/0378-3839(82)90022-9).
- [41] S. Agarwal, V. Sriram, K. Murali, Modelling Wave Interaction with Porous Structures Using Boussinesq Equations, in: *Proceedings of the Fourth International Conference in Ocean Engineering (ICOE2018)*, Springer, Singapore, 2019, pp. 573–583. [doi:10.1007/978-981-13-3119-0\\_35](https://doi.org/10.1007/978-981-13-3119-0_35).
- [42] J. Wang, Q. Ma, Numerical Investigation on Limitation of Boussinesq Equation for Generating Focusing Waves, *Procedia Engineering* 126 (2015) 597–601. [doi:10.1016/j.proeng.2015.11.310](https://doi.org/10.1016/j.proeng.2015.11.310).
- [43] Z. Liu, K. Fang, A new two-layer Boussinesq model for coastal waves from deep to shallow water: Derivation and analysis, *Wave Motion* 67 (2016) 1–14. [doi:10.1016/j.wavemoti.2016.07.002](https://doi.org/10.1016/j.wavemoti.2016.07.002).
- [44] K. Fang, Z. Liu, J. Sun, Z. Xie, Z. Zheng, Development and validation of a two-layer Boussinesq model for simulating free surface waves generated by bottom motion, *Applied Ocean Research* 94 (2020) 101977. [doi:10.1016/j.apor.2019.101977](https://doi.org/10.1016/j.apor.2019.101977).
- [45] Z. T. Yang, P. L.-F. Liu, Depth-integrated wave-current models. Part 1. Two-dimensional formulation and applications, *Journal of Fluid Mechanics* 883. [doi:10.1017/jfm.2019.831](https://doi.org/10.1017/jfm.2019.831).
- [46] B.-H. Lee, J.-C. Park, M.-H. Kim, S.-C. Hwang, Step-by-step improvement of MPS method in simulating violent free-surface motions and impact-loads, *Computer Methods in Applied Mechanics and Engineering* 200 (9-12) (2011) 1113–1125. [doi:10.1016/j.cma.2010.12.001](https://doi.org/10.1016/j.cma.2010.12.001).
- [47] A. S. Rijas, V. Sriram, S. Yan, Variable spaced particle in mesh-free method to handle wave-floating body interactions, *International Journal for Numerical Methods in Fluids* 91 (6) (2019) 263–286. [doi:10.1002/fld.4751](https://doi.org/10.1002/fld.4751).
- [48] P. Vineesh, V. Sriram, Numerical investigation of wave actions on two side by side boxes in close proximity using IMLPG.R method, *Applied Ocean Research* 116 (April) (2021) 102892. [doi:10.1016/j.apor.2021.102892](https://doi.org/10.1016/j.apor.2021.102892).
- [49] R. Divya, V. Sriram, K. Murali, Wave-vegetation interaction using Improved Meshless Local Petrov Galerkin method, *Applied Ocean Research* 101 (August 2019) (2020) 102116. [doi:10.1016/j.apor.2020.102116](https://doi.org/10.1016/j.apor.2020.102116).
- [50] G. Manoj Kumar, V. Sriram, I. Didenkulova, A hybrid numerical model based on FNPT-NS for the estimation of long wave run-up, *Ocean Engineering* 202 (October 2019) (2020) 107181. [doi:10.1016/j.oceaneng.2020.107181](https://doi.org/10.1016/j.oceaneng.2020.107181).
- [51] G. M. Kumar, V. Sriram, Development of a hybrid model based on mesh and meshfree methods and its application to fluid–elastic structure interaction for free surface waves, *Journal of Fluids and Structures* 99 (2020) 103159. [doi:10.1016/j.jfluidstructs.2020.103159](https://doi.org/10.1016/j.jfluidstructs.2020.103159).
- [52] V. Sriram, Q. W. Ma, Review on the local weak form-based meshless method (MLPG): Developments and applications in ocean engineering, *Applied Ocean Research* 116 (May). [doi:10.1016/j.apor.2021.102883](https://doi.org/10.1016/j.apor.2021.102883).
- [53] J. Bosboom, *Boussinesq modelling of wave-induced particle velocities*, Master of science, TU Delft (1995).  
URL <https://repository.tudelft.nl/islandora/object/uuid:53cd947a-1b9c-449d-bc43-325ac4397625?collection=education>
- [54] J. Bosboom, G. Klopman, J. Roelvink, J. Battjes, Wave kinematics computations using Boussinesq models, in: *Coastal Engineering 1996*, Vol. 1897, American Society of Civil Engineers, 1997, pp. 109–122. [doi:10.1061/9780784402429.009](https://doi.org/10.1061/9780784402429.009).
- [55] M. W. Dingemans, *Water Wave Propagation Over Uneven Bottoms*, Vol. 13 of Advanced Series on Ocean Engineering, World Scientific Publishing Company, 1997. [doi:10.1142/1241-part2](https://doi.org/10.1142/1241-part2).
- [56] P. Lancaster, K. Salkauskas, Surfaces generated by moving least squares methods, *Mathematics of Computation* 37 (1981) 141–158. [doi:10.1090/S0025-5718-1981-0616367-1](https://doi.org/10.1090/S0025-5718-1981-0616367-1).
- [57] B. Le Méhauté, *An Introduction to Hydrodynamics and Water Waves*, Springer Berlin Heidelberg, Berlin, Heidelberg, 1976. [doi:10.1007/978-3-642-85567-2](https://doi.org/10.1007/978-3-642-85567-2).
- [58] Kraaiennest, *Water wave theories.svg*, Wikimedia Commons, created on 2009-04-21, accessed on 2022-03-15.  
URL [https://upload.wikimedia.org/wikipedia/commons/e/e0/Water\\_wave\\_theories.svg](https://upload.wikimedia.org/wikipedia/commons/e/e0/Water_wave_theories.svg)
- [59] V. Sriram, S. A. Sannasiraj, V. Sundar, A. Schlenkhoff, T. Schlurmann, Quantification of phase shift in the simulation of shallow water waves, *International Journal for Numerical Methods in Fluids* 62 (2009) 1381–1410. [doi:10.1002/fld.2072](https://doi.org/10.1002/fld.2072).
- [60] H. Luth, G. Klopman, N. Kitou, Kinematics of waves breaking partially on an offshore bar; LDV measurements of waves with and without a net onshore current, Report H-1573, Delft Hydraulics 40.
- [61] G. Fourtakas, P. K. Stansby, B. D. Rogers, S. J. Lind, S. Yan, Q. Ma, On the coupling of incompressible SPH with a finite element potential flow solver for nonlinear free-surface flows, *International Journal of Offshore and Polar Engineering* 28 (3) (2018) 248–254. [doi:10.17736/ijope.2018.ak28](https://doi.org/10.17736/ijope.2018.ak28).
- [62] P. Brodtkorb, P. Johannesson, G. Lindgren, I. Rychlik, J. Rydén, E. Sjö, WAFO - a Matlab toolbox for the analysis of random waves and loads, in: Proc. 10<sup>th</sup> Int. Offshore and Polar Eng. Conf., ISOPE, Seattle, USA, Vol. 3, 2000, pp. 343–350.
- [63] V. Sriram, S. Agarwal, T. Schlurmann, Laboratory study on steep wave interactions with fixed and moving cylinder, *International Journal of Offshore and Polar Engineering* 31 (1) (2021) 19–26. [doi:10.17736/ijope.2021.jc808](https://doi.org/10.17736/ijope.2021.jc808).
- [64] S. Saincher, V. Sriram, S. Agarwal, T. Schlurmann, Experimental investigation of hydrodynamic loading induced by regular, steep non-breaking and breaking focused waves on a fixed and moving cylinder, *European Journal of Mechanics - B/Fluids* 93 (2022) 42–64. [doi:10.1016/j.euromechflu.2021.12.009](https://doi.org/10.1016/j.euromechflu.2021.12.009).

## Appendix A. Rectangular shell coupling interface

The 3D coupling interface can be implemented either using a cylindrical or rectangular shell, as shown in Fig. (2). The results through a cylindrical shell implementation were shown in sections 4.5 and 4.6. A similar investigation was also carried out using rectangular shell coupling interface. The test case set-up is nearly identical to section 4.5, where the hybrid model simulates the regular wave defined by case-N2 (see Table 2), propagating at an angle of 30° w.r.t to the X-axis. In this test, the cylindrical MLPG\_R sub-domain with a cuboidal MLPG\_R sub-domain having initial dimensions 7.3m × 7.3m × 1.0m is investigated. The particles are initially placed at an interval of 0.05m.

Here the coupling interface is built with buffer layers in a rectangular shell of thickness 0.15m, and relaxation zone of thickness 1m, as shown in the contour plot of the top view of MLPG\_R sub-domain, Fig. (A.28a). The resultant simulation of this case using the hybrid model leads to a failure due to poor distribution of particles at the top right corner of the MLPG\_R domain, as shown in the top view in Fig. (A.28b).

The cause of the failure was investigated by measuring relaxation function  $C$  and its gradient  $\nabla C = \frac{\partial C}{\partial x} \hat{i} + \frac{\partial C}{\partial y} \hat{j}$  along two line sections, as highlighted in Fig. (A.28a). The line-section L1 is located along the mid-line of the domain, in a region without intersection of coupling interfaces. On the other hand, line-section L2 is located in the region with intersection of coupling interfaces. Fig. (A.29) presents the plots of  $C$  and  $\nabla C$  along these line-sections. It has been observed that for L2, the  $\nabla C$  is discontinuous at the intersection of the two coupling interfaces. This discontinuity adversely impacts the  $\nabla \cdot \vec{u}$  at these regions. Further, the failure at top-right corner is due to the wave propagating at an angle of 30° w.r.t X-axis. Therefore, this top-right

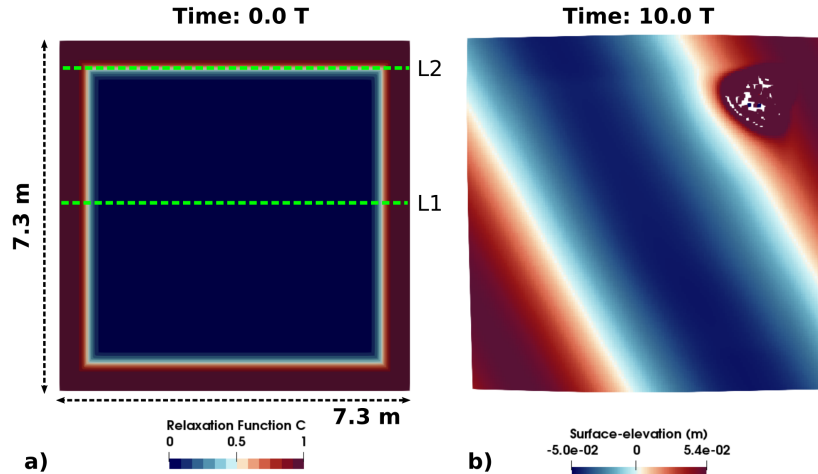


Figure A.28: Top view of the MLPG\_R sub-domain. a) Contour plot of relaxation function  $C$ , with the highlighted line-section L1 and L2 where the plots of  $C$  and  $\nabla C$  are reported in Fig. (A.29). b) Contour plot of surface-elevation  $\eta$ , showing the cause of simulation failure due to particle disturbance at top right corner.

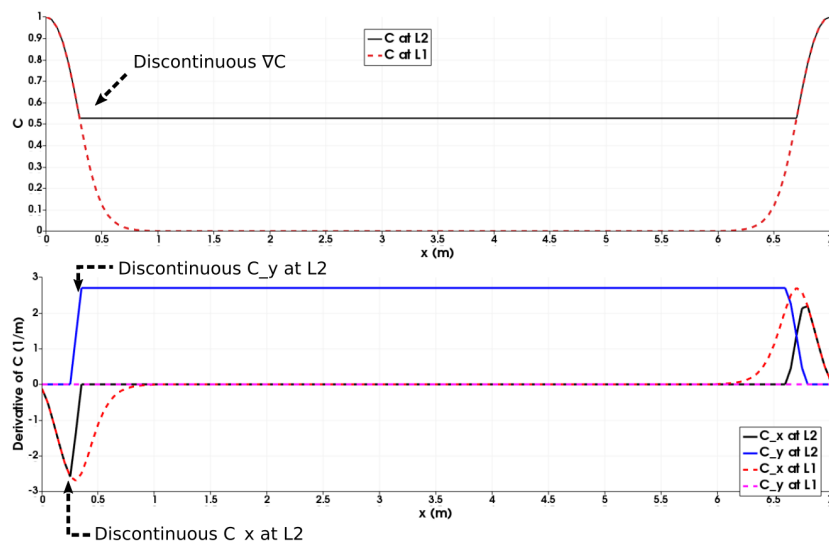


Figure A.29: Plots of relaxation function  $C$  and it's derivatives  $C_x = \frac{\partial C}{\partial x}$  and  $C_y = \frac{\partial C}{\partial y}$  along line-sections L1 and L2, highlighting the discontinuous  $\nabla C$  on L2.

corner location is downstream of the incoming wave where the difference in the velocities from the two models ( $\vec{u}_F - \vec{u}_M$ ) will be most dominant. The issue can be resolved by smoothing the intersection of the coupling interface using rounded corners, or by eliminating corner through cylindrical or ellipsoidal shells. The later was adopted in this thesis due to the robustness and applicability for wide variety of problems.